



RESEARCH ARTICLE

10.1029/2019GC008221

Key Points:

- Brine-saturated anhydrite-carbonate caprock fault gouge shows velocity-weakening friction only above 120 °C
- (Partial) saturation with methane/air shifts transition from velocity strengthening to velocity weakening to below 100 °C
- Application to seismogenic Groningen gas reservoir (100 °C) implies gas-bearing faults in overlying caprock may be earthquake prone

Supporting Information:

- Supporting Information S1
- Table S1

Correspondence to:

L. B. Hunfeld,
l.b.hunfeld@uu.nl

Citation:

Hunfeld, L. B., Chen, J., Niemeijer, A. R., & Spiers, C. J. (2019). Temperature and gas/brine content affect seismogenic potential of simulated fault gouges derived from Groningen gas field caprock. *Geochemistry, Geophysics, Geosystems*, 20, 2827–2847. <https://doi.org/10.1029/2019GC008221>

Received 23 JAN 2019

Accepted 13 MAY 2019

Accepted article online 18 MAY 2019

Published online 20 JUN 2019

Temperature and Gas/Brine Content Affect Seismogenic Potential of Simulated Fault Gouges Derived From Groningen Gas Field Caprock

Luuk B. Hunfeld¹ , Jianye Chen¹ , André R. Niemeijer¹ , and Christopher J. Spiers¹

¹HPT Laboratory, Department of Earth Sciences, Utrecht University, Utrecht, The Netherlands

Abstract We investigated the rate-and-state frictional properties of simulated anhydrite-carbonate fault gouge derived from the basal Zechstein caprock overlying the seismogenic Groningen gas reservoir in the NE Netherlands. Direct shear experiments were performed at in situ conditions of 50–150 °C and 40-MPa effective normal stress, using sliding velocities of 0.1–10 μm/s. Reservoir pore fluid compositions were simulated using 4.4 Molar NaCl brine, as well as methane, air, and brine/gas mixtures. Brine-saturated samples showed friction coefficients (μ) of 0.60–0.69, with little dependence on temperature, along with velocity strengthening at 50–100 °C, transitioning to velocity weakening at 120 °C and above. By contrast, gas filled, evacuated and partially brine-saturated samples showed μ values of 0.72 ± 0.02 plus strongly velocity-weakening behavior accompanied by stick slip at 100 °C (the only temperature investigated for gas-bearing and dry samples). A microphysical model for gouge friction, assuming competition between dilatant granular flow and thermally activated compaction creep, captures the main trends seen in our brine-saturated samples but offers only a qualitative explanation for our gas-bearing and dry samples. Since the reservoir temperature is ~100 °C, our results imply high potential for seismogenic slip nucleation on faults that cross cut and juxtapose the basal Zechstein anhydrite-carbonate caprock against the Groningen reservoir sandstone, specifically in the gas-filled upper portion of the reservoir system.

Plain Language Summary Rock formations composed of calcium sulfate and carbonate salts overly and seal many oil and gas reservoirs around the world. Faults cutting such formations may be reactivated in response to hydrocarbon extraction, potentially causing *induced* earthquakes. We investigated the frictional behavior of simulated faults in the sulfate/carbonate-rich basal Zechstein formation, which overlies Europe's largest gas reservoir (Groningen gas field, the Netherlands) where substantial induced seismicity has occurred in recent years. This was done by means of experiments where we simulate the sliding motion of faults, while varying the temperature and fluid content of the crushed rock products within the fault. The experiments were done at true subsurface reservoir conditions. Our results show that when faults are saturated with brine filling the bottom of the sandstone reservoir layer, they become prone to generating earthquakes at temperatures of 120 °C and above, whereas when they are saturated with gas or gas/brine mixtures characterizing the top of the reservoir system, this already occurs at 100 °C. Since the temperature in the Groningen reservoir is ~100 °C, our results and supporting theoretical calculations imply that earthquake nucleation is most likely to occur on faults that incorporate basal Zechstein-derived material, specifically in the gas-filled, upper portion of the reservoir.

1. Introduction

Evaporite formations, containing thick deposits of interbedded anhydrite and carbonates at their base, are common in sedimentary basins and frequently form the top seal of hydrocarbon reservoirs. Prominent examples include the Zechstein sequence overlying the Rotliegend gas fields in the Netherlands and North Sea (Geluk, 2007) and the Sudair Formation capping the Khuff gas fields in Qatar (Alsharhan & Nairn, 1994). Hydrocarbon production often induces modest seismicity (e.g., Segall, 1989), by reactivating faults that cross cut the reservoir and adjacent formations. The potential for a fault to generate an earthquake is related to its capacity to weaken once motion is initiated on the fault. This can be achieved by slip weakening, that is, a decrease in frictional strength with increasing displacement, leading to accelerating slip and thus seismogenesis (Andrews, 1976; Ida, 1972). Another possibility is that of fault weakening as motion accelerates or *velocity-weakening* behavior (Dieterich, 1979; Ruina, 1983; Scholz, 2002). By contrast, if the frictional strength of a fault increases with ongoing slip and/or increasing slip velocity, via slip-hardening

©2019. The Authors.

This is an open access article under the terms of the Creative Commons Attribution-NonCommercial-NoDerivs License, which permits use and distribution in any medium, provided the original work is properly cited, the use is non-commercial and no modifications or adaptations are made.

or *velocity-strengthening* behavior, the fault is likely to exhibit aseismic slip. The mechanical stability of faults, that is, whether they accommodate unstable seismic rupture versus stable (aseismic) slip, is therefore in part controlled by the reactivation and frictional slip behavior of the fault gouge present in the faults (Scholz, 2002; Tse & Rice, 1986). In particular, to understand fault stability and the potential for seismogenesis in anhydrite-carbonate caprocks topping producing hydrocarbon reservoirs, the mechanisms that control the displacement- and velocity-dependent frictional properties of anhydrite-carbonate fault gouges must therefore be addressed. The same applies to assessing the risks of seismicity associated with gas (CO₂ or H₂) storage in depleted reservoirs. Data on such gouges are also highly relevant to natural seismicity occurring in tectonically active evaporite terrains, such as in the Italian Apennines (Collettini et al., 2009; Speranza & Minelli, 2014).

The present paper focuses on the basal Zechstein formation, a ~50-m thick sequence of interbedded anhydrites and carbonates that overlies the Groningen gas field located in the north-east of the Netherlands (Geluk, 2007) at a depth of ~3 km. Gas production from this onshore field, the seventh largest in the world, has led to significant induced seismicity since the 1990s (van Thienen-Visser & Breunese, 2015), raising major public concern. Relatively little is known about the frictional properties of faults cutting the Groningen reservoir system. Recently, Hunfeld et al. (2017) investigated the frictional properties of simulated fault gouges derived from the main lithologies present in the Groningen gas reservoir system, under brine-saturated conditions (i.e., pore space 100 % brine filled), at an in situ temperature of 100 °C and an effective normal stress of 40 MPa. In their work, the top of the Groningen reservoir system, including the basal Zechstein caprock, was identified as potentially having velocity-weakening frictional properties that are conducive to seismogenic slip nucleation (Hunfeld et al., 2017). In the present paper, we further investigate the frictional properties of anhydrite-carbonate gouges prepared from the basal Zechstein, focusing on the full range of temperatures and gas/brine saturation levels relevant to faults cutting this unit.

With these aims, we performed direct shear experiments on simulated anhydrite-carbonate-rich fault gouge derived from core taken from the basal Zechstein in the center of the Groningen field. Direct shear, velocity-stepping experiments were performed on samples saturated with simulated reservoir brine (4.4 Molar NaCl solution) and on samples saturated with CH₄, air, and gas/brine mixtures, mimicking the methane/nitrogen-rich environment in the upper part of the reservoir system, that is, above the gas-water contact (De Jager & Geluk, 2007). The experiments were conducted at simulated reservoir conditions, that is, at 100 ± 50 °C, 40 MPa effective normal stress, and pore pressures between atmospheric and 15 MPa. The sliding velocities employed (0.1–10 μm/s) simulate the nucleation stage of fault slip (Scholz, 2002). We analyzed the velocity dependence of friction as a function of temperature and pore fluid composition, using the classical rate-and-state friction (RSF)-dependent model of Dieterich (1978, 1979) to describe our data empirically. In addition, we applied a microphysical model for gouge friction, recently developed at our laboratory, in an attempt to explain the mechanisms controlling the main trends seen in the experimental data.

2. Experimental Materials and Methods

2.1. Sample Material

The sample material used in this study was identical to the simulated basal Zechstein gouge used by Hunfeld et al. (2017). Drill cuttings of the basal Zechstein were obtained from the Zeerijp-02 (ZRP-02) research well (2015), located in the central part of the Groningen field, courtesy of the Nederlandse Aardolie Maatschappij BV. The drill cuttings were retrieved from a depth interval of 2,870–2,905 m. Note that the ZRP-02 well does not penetrate any seismically visible fault zones in this depth interval, so that the cuttings are assumed to reflect the composition of the (intact) basal Zechstein unit. The drill cuttings were hand crushed with a pestle and mortar and sieved to a grain size <50 μm, simulating the fine-grained gouge material present in the principal slip zones of typical natural fault zones at shallow crustal depths (De Paola et al., 2008; Sibson, 1986). The grain size distribution of the crushed and sieved sample material, measured using a Malvern laser particle sizer, showed a median particle diameter (d_{50}) of 7.2 μm. Conventional X-ray diffraction analysis performed on the simulated fault gouge [see Hunfeld et al., 2017] revealed that it consists predominantly of anhydrite (48 wt %), carbonates (32 wt % calcite and dolomite), and barite (14 wt %), with minor amounts (<10 wt %) of quartz.

Table 1
List of Experiments, Conditions and Key Data

Exp. No.	T (°C)	P _c (MPa)	P _f (MPa)	Pore fluid	L _i (mm)	L _f (mm)	μ _{2mm} (–)	D _{tot} (mm)	V-dep.
Brine-saturated experiments									
Z2BZ-26	50	55	15	4.4 M NaCl	1.05	0.75	0.691	5.36	V _s
Z2BZ-25	80	55	15	4.4 M NaCl	1.10	0.80	0.632	5.49	V _s
Z2BZ-06	100	55	15	4.4 M NaCl	1.00	0.80	0.637	5.50	V _s
Z2BZ-17	120	55	15	4.4 M NaCl	1.10	0.73	0.599	5.51	V _s
Z2BZ-08	150	55	15	4.4 M NaCl	1.05	0.70	0.621	5.43	V _w /V _s
Z2BZ-22 ^a	100	55	15	4.4 M NaCl	1.15	0.80	0.641	5.50	V _w /V _s
Dry and partially saturated experiments									
Z2BZ-27	100	40	-	Vacuum	1.05	0.93	0.720	5.20	V _w
Z2BZ-07	100	40	Atm.	Air	1.00	0.90	0.744	5.37	V _w
Z2BZ-13	100	50	10	CH ₄	1.05	0.88	0.734	5.42	V _w
Z2BZ-15	100	40	Atm.	Air + 4 M NaCl ^b	1.05	0.73	0.721	5.40	V _w
Z2BZ-12	100	50	10	CH ₄ + 4 M NaCl ^b	1.00	0.85	0.696	5.39	V _w /V _s

Note: Symbols and coding: T = temperature; P_c = confining pressure; P_f = pore fluid pressure; Atm. denotes atmospheric pressure; L_i = initial layer thickness; L_f = final layer thickness; μ_{2mm} = friction coefficient obtained at ~2-mm shear displacement; D_{tot} = total shear displacement; V-dep. denotes velocity dependence; V_s and V_w indicate velocity-strengthening and velocity-weakening behavior, respectively.

^aThis experiment used an alternative velocity-stepping scheme. See section 3.2. ^bPartially saturated samples: 17–34 vol% of the pore volume is filled with brine, and 66–83 vol% with air or CH₄.

2.2. Direct Shear Experiments

We conducted 11 velocity-stepping, direct shear friction experiments on ~1-mm thick layers (width 35 mm × 48 mm length) of simulated fault gouge. Six of these were performed on samples saturated with a 4.4 Molar (M) NaCl brine, simulating the highly saline formation water present in the reservoir, varying temperature in the range 50–150 °C. The remainder were conducted at 100 °C (approximately the reservoir temperature) under varying pore fluid conditions, that is, with the pores (a) filled (saturated) with and drained to lab air, (b) saturated with CH₄ at elevated pressure, or (c) containing pressurized mixtures of either air or CH₄ with brine. Runs performed using these mixtures will be referred to as partially saturated experiments, whereby 17–34 vol% of the pore volume was filled with brine, and 66–83 vol% with air or CH₄. These percentages are based on mass and sample dimension measurements made before and after testing, assuming no loss of solid or liquid. The ratio 17:83 vol% reflects the saturation level (liquid:gas content) immediately after sample assembly (before application of normal stress or shear deformation), while that of 34:66 vol% represents the saturation ratio measured after completion of the experiments. The pore fluids used simulate those present in the gas-filled, upper portion of the reservoir system (Burkitov et al., 2016). A single control experiment was run *dry*, with the pore fluid system under vacuum. All experiments were performed at an effective normal stress (σ_n^{eff}) of 40 MPa. In the case of samples saturated with brine, a pore fluid pressure (P_f) of 15 MPa was used. Experiments employing CH₄ as pore fluid were done using a gas pressure of 10 MPa. Atmospheric pore pressure was used in experiments with lab air. Table 1 lists all experiments conducted and the applied conditions.

2.2.1. Experimental Setup and Gouge Layer Preparation

The experiments were performed using a conventional triaxial testing machine referred to as the Shuttle apparatus, equipped with a polymer-jacketed direct shear assembly enclosing the gouge sample [see Verberne et al., 2013]. The apparatus consists of an internally heated, constant volume triaxial pressure vessel with silicon oil as the confining medium, mounted in an Instron 1362 servo-controlled loading frame. In the Shuttle apparatus, axial force is transmitted to the sample via a Ti-grade 5 driving piston equipped with a fully internal differential variable reluctance transformer with 100 kN full scale and ±33 N resolution, to measure axial force independent of seal friction. Axial displacement of the driving piston is measured externally using a linear variable differential transformer with 100-mm full scale and ±1.5-μm resolution. Confining pressure and pore fluid pressure are maintained constant throughout the experiment (to within ±0.00138 MPa), and oil volume and pore fluid volume are measured, using two independent Teledyne ISCO D65 syringe pumps (150 MPa range), with built-in Honeywell pressure transducers for both control and pressure measurement. The vessel is heated by means of a Thermocoax internal furnace and controlled using a three-term CAL2300

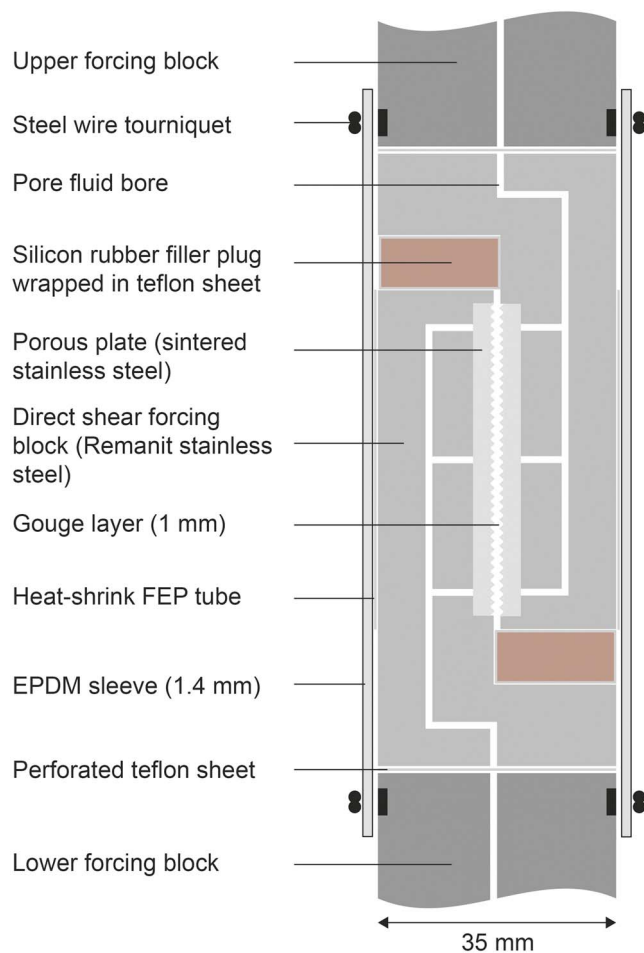


Figure 1. Schematic diagram of the direct shear setup at the start of the experiments. Axial shortening produces shear of the gouge layer and extrusion of the silicon rubber filler plugs. EPDM = ethylene-propylene diene monomer; FEP = fluorinated ethylene propylene.

industrial controller, allowing temperature control to within 0.1 °C. Sample temperature is measured using an inconel-sheathed, K-type (chromel/alumel) thermocouple in a position adjacent to the sample layer.

The direct shear assembly consists of two L-shaped forcing blocks sandwiching a ~1-mm thin layer of gouge material as shown in Figure 1 (see Samuelson & Spiers, 2012 for a detailed description of the direct shear assembly). The normal stress (σ_n) acting on the sample layer in this setup is constant, and at all times equal to the confining pressure (P_c), independent of shear displacement. The layers were prepared by distributing ~3.2 g of dry powder evenly over one of the grooved forcing block interfaces, which was then prepressed in a hydraulic press at ~30 MPa for 2 min, resulting in layers of 1.0- to 1.1-mm thickness, with porosities in the range of 35–45%. The partially saturated gouge layers of experiments Z2BZ-12 and Z2BZ-15 were prepared as a mouldable paste, created by mixing dry gouge material with 0.7 M NaCl solution in the proportion 4:1, which was then distributed over the grooved interface of one of the forcing blocks forming a ~1-mm thick layer. The sample was then oven dried at 75 °C until only ~17% of the pore volume was saturated with the fluid, monitored by intermittent weighing of the sample. At that stage, the remaining pore fluid had a salinity of ~4 M.

After preparing the gouge layers, the second direct shear forcing block was put into place, and the sample was jacketed in a thin fluorinated ethylene propylene sleeve for support. The gaps present at each end of the gouge layer (see Figure 1) were filled with half-cylindrical plugs of extremely soft silicon rubber (Ecoflex 00-20), wrapped in polytetrafluorethylene sheets. This ensured that confining pressure was transmitted uniformly to the sample, while allowing shear displacement (i.e., axial shortening of the assembly and extrusion of the silicon rubber plugs) with negligible resistance. Finally, the entire assembly was jacketed in an ethylene-propylene diene monomer sleeve of ~1.4-mm thickness, which was sealed against the load-transmitting driver blocks of the Shuttle apparatus by means of steel wire tourniquets. Circular polytetrafluorethylene sheets with holes for pore fluid access were inserted at the base of each direct shear forcing block to reduce friction between the forcing blocks and the driver blocks.

2.2.2. Experimental Procedure

The jacketed sample assembly was loaded in the Shuttle vessel, and the pore fluid system was evacuated for ~25 min before inserting the chosen pore fluid. In the case of experiments Z2BZ-12 and Z2BZ-15, the pore fluid system was not evacuated, to prevent further drying of the partially saturated samples. Samples employing CH₄ as a pore fluid were flushed with gas straight from the supply bottle connected to the pore fluid system. After inserting the pore fluid, the desired confining pressure (P_c) and pore fluid pressure (P_f) were applied, and the vessel was heated to the desired temperature (T). Experiment Z2BZ-07 (tested with lab air) was the only one that was heated with the pore fluid system drained to lab air. All other tests were heated with a closed pore fluid system, filled with brine, gas, a gas-brine mixture, or under vacuum.

After equilibration of the sample and machine at the desired confining pressure, pore pressure, and temperature conditions (after 4–6 hr), shearing of the gouge was initiated by advancing the loading ram at a constant load-point displacement rate (V) of 5.4 $\mu\text{m/s}$, until a steady state shear strength was reached at 1- to 2-mm shear displacement. Velocity steps to 0.1-1-10-0.1-1-10 $\mu\text{m/s}$ were then imposed, each over a displacement interval of 0.3–0.7 mm. Upsteps of 0.1–1 and 1–10 $\mu\text{m/s}$ were thus repeated in each experiment. A single experiment (Z2BZ-22) on a brine-saturated sample was performed using a velocity-stepping scheme of 5.4-0.01-0.1-1-10-100 $\mu\text{m/s}$. Total shear displacements (D_{tot}) of 5.4–5.9 mm were reached in each experiment (Table 1).

After extraction of the sample assembly from the vessel, the final layer thickness was measured using a caliper, and intact sample fragments were recovered for microstructural analyses, flushed with demineralized water, dried at 50 °C, and then impregnated with Araldite 2020 epoxy resin. Sections of the impregnated fragments were cut in an orientation parallel to the shear direction and perpendicular to the shear plane. These were examined by means of scanning electron microscopy, performed using an FEI Helios 650UC focused ion beam-scanning electron microscope. Imaging was done in backscattered electron mode, using an acceleration voltage of 5–15 kV.

2.3. Data Acquisition and Analysis

During the experiments, axial load, axial piston, hence direct shear displacement, confining pressure, temperature, and pore fluid volume and pressure signals were logged at a rate of 10–100 Hz using a National Instruments, 16-bit A/D data acquisition system and VI logger software. The raw data were processed to obtain shear stress τ (MPa), effective normal stress $\sigma_n^{\text{eff}} = P_c - P_f$ (MPa) and apparent friction coefficient $\mu = \tau/\sigma_n^{\text{eff}}$ (–) (Byerlee, 1978) versus displacement and time. Predetermined calibrations using a steel dummy of known elastic properties were used to correct the recorded displacement data for elastic distortion of the testing machine. Gouge sample permeability was sufficiently high, and thickness was sufficiently low to ensure fully drained behavior during steady state shearing of brine-saturated samples at the sliding velocities used. In experiments performed on brine-saturated samples, we were therefore able to use the pore fluid (ISCO pump) volume data, corrected for leak rate and changes in density of the pore fluid with temperature, to obtain gouge pore volume changes, hence layer dilatation/compaction data during steady state shear (assuming negligible change in solid volume). This was not possible for experiments employing CH₄, air or vacuum, due to high and variable leak rates in the pore fluid system and/or the absence of pore fluid pressure control. The maximum absolute error due to transducer resolution for the key quantities obtained in the experiments was ± 0.003 in friction coefficient (μ), $\pm 1.5 \mu\text{m}$ in shear displacement (D), and $\pm 3 \mu\text{m}$ in dilatation/compaction (ΔL). Note, however, that the uncertainty in μ due to experimental reproducibility in similar direct shear friction experiments is typically ± 0.02 (e.g., Hunfeld et al., 2017).

The rate dependence of friction was obtained from our velocity-stepping tests using the Dieterich-type RSF formulation (Dieterich, 1978, 1979), given

$$\mu = \mu_0 + a \cdot \ln\left(\frac{V}{V_0}\right) + b \cdot \ln\left(\frac{V_0 \theta}{d_c}\right) \quad (1)$$

$$\frac{d\theta}{dt} = 1 - \frac{V\theta}{d_c} \quad (2)$$

These equations describe the evolution of the friction coefficient from a reference steady state value (μ_0) toward a new steady state value (μ) over a critical slip distance (d_c), in response to an instantaneous change in sliding velocity from an initial velocity (V_0) to a new velocity (V). The direct effect, a , describes the instantaneous response in friction upon a stepwise change in sliding velocity, while b describes the evolution in friction toward a new steady state strength. The state variable θ describing this evolution is commonly viewed as the average lifespan of a population of grain-to-grain contacts (Marone, 1998). At steady state, that is, when $d\theta/dt = 0$ in equation (2), equation (1) reduces to

$$(a-b) = \frac{\mu - \mu_0}{\ln(V/V_0)} \quad (3)$$

defining the rate-sensitivity parameter ($a-b$). Positive values of ($a-b$) indicate velocity-strengthening behavior, whereas negative values indicate velocity-weakening behavior. The interaction of the sample with its elastic surroundings is accounted for via the relation

$$\frac{d\mu}{dt} = k(V_{\text{lp}} - V) \quad (4)$$

where k is the stiffness of the fault surroundings (i.e., the gouge layer plus shear apparatus in experiments) normalized by the normal stress, V_{lp} is the load-point velocity, and V is the true (gouge) slip velocity.

Values for the rate-sensitivity parameter ($a-b$) and the individual constitutive parameters a , b , and d_c were determined by fitting the data with the widely used inverse modeling technique following the approach described by Blanpied et al. (1998). Fitting the data using the Ruina-type RSF formulation (Marone, 1998) instead of the Dieterich-type formulation yields the same results for values of ($a-b$). In the case of stick-slip behavior, modeling of the data was unsuccessful, and ($a-b$) was determined manually using equation (3), taking the peak μ attained during stick slip to define μ and μ_0 at sliding velocities V and V_0 .

3. Results

3.1. Friction Coefficient Versus Displacement

Key data obtained per experiment are listed in Table 1. The evolution of μ with displacement for brine-saturated experiments performed at varying temperature and for the runs conducted with different pore fluid composition are shown in Figures 2a and 2b, respectively. All experiments showed a rapid, near-linear increase in shear stress for the first ~ 0.5 mm of displacement, followed by hardening at decreasing rate toward a peak frictional strength attained at 1–2 mm of displacement. Beyond the peak, most experiments showed minor, near-linear displacement weakening, with superimposed steps in frictional strength in response to velocity steps. Experiments performed on brine-saturated samples (Figure 2a) showed stable sliding behavior at all temperatures and velocities investigated, except for Z2BZ-08 at 150 °C, which showed minor stick-slip behavior at 0.1 $\mu\text{m/s}$, the lowest velocity investigated. The background weakening rate increased with temperature, being most pronounced at temperatures >100 °C. Samples tested at 100 °C but only partially saturated with brine (Figure 2b) also showed stick slip only at 0.1 $\mu\text{m/s}$. Gas-saturated and evacuated samples tested at 100 °C (Figure 2b) showed more prominent stick-slip behavior, notably at the lower sliding velocities investigated, transitioning to stable sliding at 10 $\mu\text{m/s}$ in the case of samples tested with air or under vacuum. Stick-slip stress drops in these samples were largest at the lowest velocities imposed (1–2 MPa at 0.1 $\mu\text{m/s}$, corresponding to friction drops of ~ 0.03 – 0.05), decreasing in magnitude not only toward higher velocity but also with increasing displacement.

Focusing on the general level of friction strength, μ values determined for the brine-saturated gouges at 2-mm displacement and 5.4 $\mu\text{m/s}$ varied from 0.69 at 50 °C to 0.62 ± 0.02 at 80–150 °C (Table 1). Samples partially saturated with brine were significantly stronger, with μ values at 2-mm displacement of 0.71 ± 0.01 . The gas-saturated and evacuated gouges were stronger still, showing friction coefficients of 0.73 ± 0.01 at ~ 2 -mm displacement (Table 1). Amongst these, the sample tested with CH_4 behaved very similarly to those tested with air or under vacuum.

3.2. Rate Dependence of Friction

The values of the RSF parameters a , b , d_c and ($a-b$) obtained from all velocity steps in our experiments are presented in the supporting information Table S2. We plot ($a-b$) for all velocity steps in all experiments in Figure 3.

The brine-saturated gouges (Figures 3a and 3b) showed mostly positive ($a-b$) values at 50–120 °C, demonstrating velocity-strengthening behavior. Going from 50 to 80 °C, a slight increase in ($a-b$) was observed for most velocity steps. However, beyond 80 to 100 °C, ($a-b$) systematically decreased with increasing temperature, attaining negative velocity-weakening values in downsteps from 5.4 to 0.1 $\mu\text{m/s}$ at 120 and 150 °C, and in upsteps from 0.1 to 1 $\mu\text{m/s}$ at 150 °C. At any given temperature, all experiments on brine-saturated gouges also showed an increase in ($a-b$) with increasing load-point velocity, specifically in velocity upsteps. Figure 3b shows this trend explicitly for run Z2BZ-22, across 4 orders of magnitude in (poststep) load-point velocity at 100 °C. The individual a , b , and d_c values obtained in this experiment also showed trends with sliding velocity (Figure 3b). The direct effect a did not change with velocity up to 10 $\mu\text{m/s}$ but more than doubled for the fastest upstep (10–100 $\mu\text{m/s}$). The evolution effect b showed a near log-linear decrease with increasing velocity, attaining negative values in upsteps beyond 10 $\mu\text{m/s}$. The critical slip distance d_c increased with velocity, from ~ 2 μm at 0.1 $\mu\text{m/s}$ to ~ 450 μm at 100 $\mu\text{m/s}$. All brine-saturated samples showed similar trends in the RSF parameters with velocity (see Table S1). By contrast, no systematic trends in a , b , or d_c were observed with respect to temperature or shear displacement, in any of the brine-saturated runs.

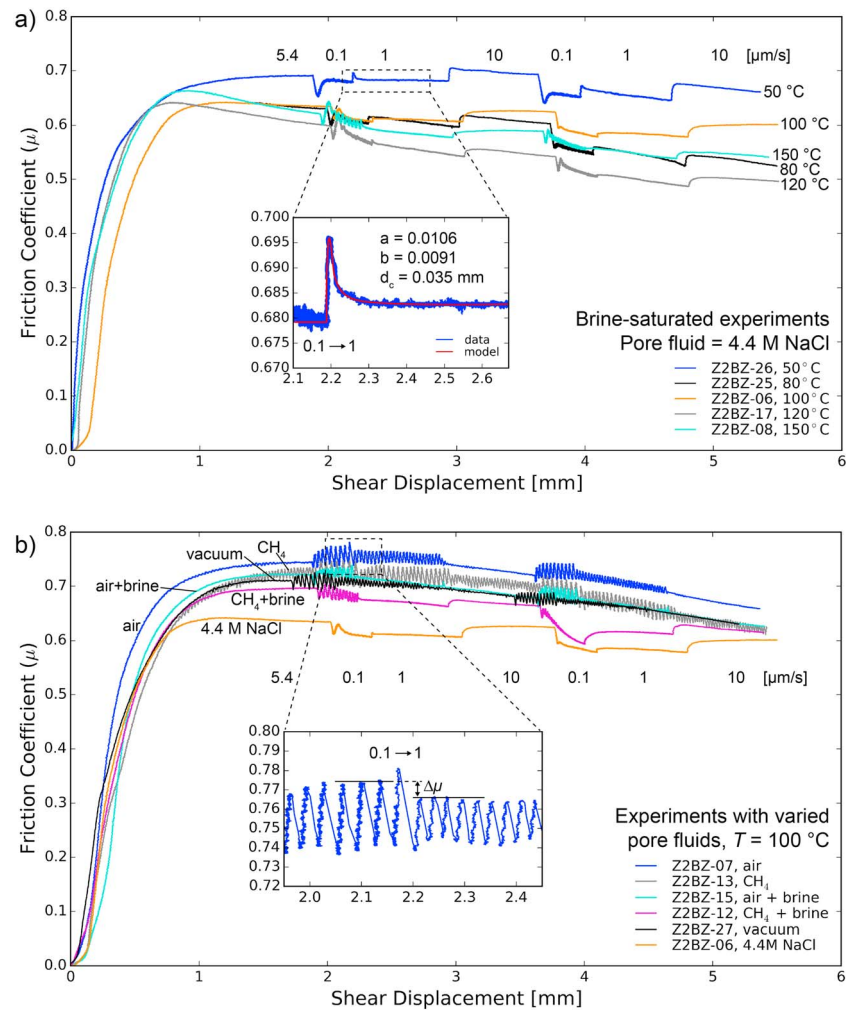


Figure 2. Friction coefficient μ versus shear displacement curves for (a) brine-saturated samples tested at 50–150 °C and (b) samples tested at 100 °C with methane/air, brine/gas mixtures, and under vacuum. The inset in Figure 2a shows an RSF inversion fit to a velocity step in a brine-saturated sample. That in Figure 2b shows stick slips in a gouge saturated with air. The load-point velocities applied are as indicated per step. Effective normal stress was 40 MPa in all experiments (see Table 1). RSF = rate-and-state friction.

In the experiments conducted with different pore fluids at 100 °C, samples saturated with air, CH_4 , or tested under a vacuum, as well as samples partially saturated with brine, showed very similar, strongly negative ($a-b$) values in almost all velocity steps (Figure 3c). This is consistent with the prominent stick-slip behavior observed in these experiments (Figure 2b). Significant positive ($a-b$) values were only observed for upsteps applied in experiment Z2BZ-12 (tested with CH_4 plus brine). Unlike the brine-saturated samples, the partially saturated, gas-bearing and evacuated samples showed no systematic dependence of ($a-b$) on load-point velocity. Trends in the individual RSF parameters could not be determined for these samples due to the widespread stick slip.

3.3. Sample Thickness Changes

Direct thickness measurements after sample extraction showed a reduction in layer thickness with respect to the starting layer thickness in all samples (Table 1). The mean thickness change for brine-saturated samples was $\sim 0.3 \text{ mm}$, corresponding to $\sim 25\%$ porosity reduction, assuming no sample extrusion. This reflects both porosity reduction during system equilibration at the applied normal stress prior to shearing, as well as compaction during shear and minor expansion upon vessel depressurization. The mean thickness change for samples saturated with air, CH_4 , or under vacuum was $\sim 0.15 \text{ mm}$, approximately half the thickness

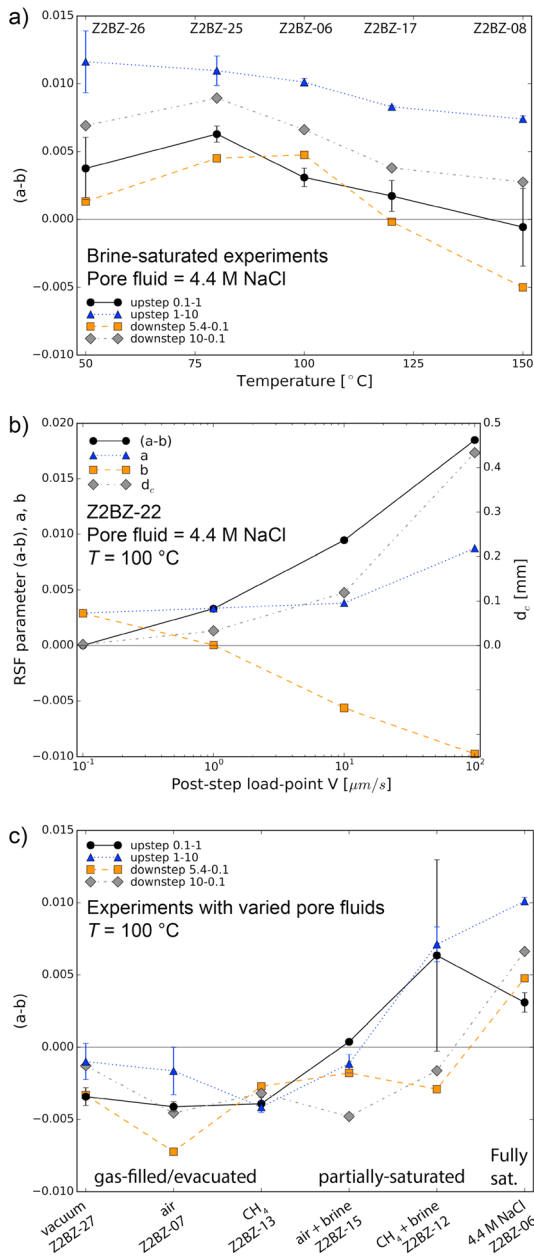


Figure 3. (a) $(a-b)$ values for all velocity steps performed using brine-saturated samples plotted versus temperature. (b) RSF parameters determined in brine-saturated experiment Z2BZ-22 plotted versus poststep load-point velocity. Note that in this experiment we employed velocity steps covering the range 0.01–100 $\mu\text{m/s}$. The results show relatively little change in a but continuously decreasing b with increasing velocity, resulting in $(a-b)$ values that increase with sliding velocity. The critical slip distance d_c also increased with velocity, from $\sim 2 \mu\text{m}$ for the slowest step (0.01–0.1 $\mu\text{m/s}$) to $\sim 430 \mu\text{m}$ for the fastest step (10–100 $\mu\text{m/s}$). (c) $(a-b)$ data for the samples at 100 °C plotted versus pore fluid condition, including brine-saturated experiment Z2BZ-06 for comparison. Note that for upsteps in velocity, we plot the average $(a-b)$ value determined from repeated velocity steps, with the error bars showing the range of values obtained for these steps. RSF = rate-and-state friction.

change in brine-saturated samples. Partially saturated samples showed a mean thickness change of $\sim 0.21 \text{ mm}$, so approximately two thirds of that for fully brine-saturated samples.

Continuous pore volume change, hence gouge layer thickness change data, was successfully obtained only for the brine-saturated samples tested at 50, 80, and 120 °C due to a later-discovered error in the data acquisition system. These samples showed steady, ongoing compaction during shear marked by transiently enhanced compaction in response to velocity downsteps and minor transient dilatation upon upstepping. An example is given in Figure 4a, showing the evolution of friction and gouge layer compaction with displacement at 120 °C. Steady state compaction rates could only be reliably estimated during the slowest velocity intervals (0.1 $\mu\text{m/s}$). These are plotted in Figure 4b for the experiments done at 50, 80, and 120 °C and showed a roughly Arrhenius dependence on temperature suggesting an apparent activation energy for the compaction process of $10 \pm 6 \text{ kJ/mol}$ at the 40-MPa effective normal stress used in all tests.

3.4. Microstructures

Brine-saturated samples showed essentially the same microstructure at all temperatures investigated (50–150 °C). Fine-grained R1 Riedel shear bands (terminology after Logan et al., 1979) and continuous boundary (B) shears, located near the sample margin, developed in all of these samples, with an irregular and variable width of 10–30 μm (Figures 5a–5c). R1 spacing in the shear direction was $\sim 1.5 \text{ mm}$. The main gouge body shows a broad grain size distribution with numerous angular clasts of quartz, carbonates, and barite similar in size to the coarsest grains in the starting material (20–50 μm), embedded in a cataclastically refined matrix (~ 1 –5 μm). Fractured and comminuted grains are observed throughout the bulk of the gouge, with the carbonate and sulfate grains showing preferential grain size reduction compared with quartz. The B and R1 shear bands are characterized by extreme grain size reduction compared with the bulk gouge (Figure 5c), with most particles in the shear bands being less than 1 μm in diameter. The shear bands exhibit a relatively dense, granular microstructure with more rounded grains compared to the gouge bulk (Figure 5c).

The gas-bearing and evacuated samples show a similar microstructure to the brine-saturated samples but with broader zones of localization (Figures 5d–5f). The shear bands in these samples are generally much wider (50 to 300 μm) and more closely spaced ($\sim 1 \text{ mm}$) than in the brine-saturated samples and show a more chaotic, more porous microstructure with a larger proportion of relatively coarse clasts (Figures 5e and 5f). In addition to R1 and B shears, these samples also show Y shears (Figure 5d) that link up with or terminate at R1 shears.

4. Discussion

The present results demonstrate clear effects of temperature and pore fluid saturation conditions, that is, gas/brine ratio, on the frictional properties of simulated anhydrite-rich fault gouges prepared from basal Zechstein caprock from the Groningen gas field. In terms of frictional strength, brine-saturated samples showed friction coefficients of 0.60–0.69, which are closely similar to previously reported values for the same

(brine-saturated) gouge composition (Hunfeld et al., 2017) and for wet anhydrite, calcite, and dolomite gouges in general (e.g., Pluymakers et al., 2016; Scuderi et al., 2013). When only partially saturated with

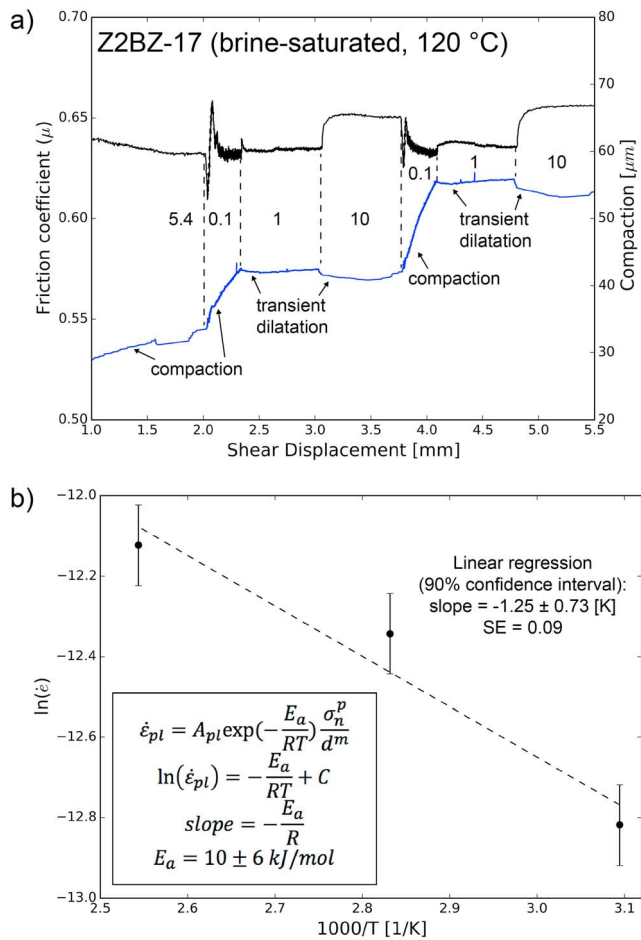


Figure 4. (a) Friction coefficient (black line, left-hand axis) and gouge layer compaction (blue line, right-hand axis) versus displacement for a brine-saturated sample at 120 °C (run Z2BZ-17). Note that friction data are corrected for linear displacement-weakening trends. Sliding velocities are indicated in $\mu\text{m/s}$. (b) Arrhenius-type diagram plotting the logarithm of gouge compaction creep rate, determined from compaction versus time data obtained in the 0.1 $\mu\text{m/s}$ sliding velocity intervals imposed in experiments on brine-saturated samples at 50, 80, and 120 °C. The slope is determined by linear regression with 90% confidence interval and is used to estimate the apparent activation energy (E_a) in equation 6a, as shown in the inset. Recall that all experiments were performed at 40-MPa effective normal stress.

brine, or when aqueous pore fluids are absent, frictional strength is significantly higher (0.70–0.74), in agreement with the results of Verberne et al. (2013) and Pluymakers, Samuelson, et al. (2014) for nominally dry calcite and anhydrite gouges. The simulated basal Zechstein gouge is thus significantly stronger than gouges prepared from the underlying claystone, sandstone, and shale formations of the Groningen field, which, respectively, exhibit friction coefficients of 0.35–0.38, 0.59–0.62, and 0.49–0.50 under brine-saturated conditions [see Hunfeld et al., 2017].

In addition, our results for basal Zechstein gouge at 100 °C showed that under partially brine-saturated and dry conditions (including CH_4 -rich environments), the velocity dependence of friction is strongly negative (Figure 3c), favoring nucleation of accelerating slip. By contrast, brine-saturated samples showed stable velocity-strengthening behavior at temperatures of 50–100 °C (Figure 3a), transitioning to velocity-weakening slip at temperatures ≥ 120 °C, or perhaps lower at sliding velocities below the minimum of 0.1 $\mu\text{m/s}$ investigated here (Figure 3b). A similar transition was observed in previous experiments on fluid-saturated fault gouges composed of calcite, anhydrite, or dolomite [Chen et al., 2015; Pluymakers, Samuelson, et al., 2014, 2016; Scuderi et al., 2013; Verberne et al., 2013], pointing to the importance of chemically assisted, thermally activated mechanism(s) in controlling slip stability for these materials.

In the following, we aim to explain the effects observed in our experiments. To aid in this, we make use of the microphysical model for gouge friction developed by Niemeijer and Spiers (2006, 2007) and Chen and Spiers (2016), referring to it as the Chen-Niemeijer-Spiers (CNS) model. We focus on analyzing and explaining the mechanisms controlling the frictional behavior seen in the brine-saturated experiments by quantitative comparison with this model. A more qualitative approach is adopted for the gas-bearing and evacuated samples. Finally, we discuss the implications of our results in the context of (induced) seismicity in the Groningen gas field and in evaporite and limestone terrains in general.

4.1. Introduction to the CNS Model

The velocity dependence of friction is classically described by the empirical RSF equations (Dieterich, 1978, 1979; Ruina, 1983). These have been highly successful in reproducing fault slip behavior observed in experiments at low (rupture nucleation) velocities (e.g., Blanpied et al., 1998; Tullis & Weeks, 1986), as well as in simulating the seismic cycle and after-shock behavior of active faults in nature (e.g., Dieterich, 1994; Kato & Tullis, 2003). However, the large variations in RSF parameters with tem-

perature, sliding velocity, normal stress, and pore fluid composition that are widely observed in experiments [e.g., Blanpied et al., 1995; Boulton et al., 2014; Carpenter et al., 2016; Chester, 1994; den Hartog & Spiers, 2013; Ikari et al., 2009; Pluymakers, Samuelson, et al., 2014; Scuderi et al., 2013; Shimamoto, 1986; Verberne, 2015] are neither explained nor captured in the classical RSF framework. To bridge this gap, mechanism-based models have recently begun to appear that aim to provide a microphysical basis for describing the frictional behavior of fault gouges and for underpinning the phenomenological RSF equations (Aharonov & Scholz, 2018; Chen & Spiers, 2016; den Hartog & Spiers, 2014; Ikari et al., 2016; Niemeijer & Spiers, 2007). The advantage of these is that they can be used to model fault behavior beyond laboratory conditions, for example, to extrapolate to natural temporal and spatial scales on the basis of the operation of observed deformation mechanisms in both laboratory and nature. We use the most recent version of the CNS model [see Chen & Spiers, 2016; Chen et al., 2017] in the present paper.

The model assumes an idealized microstructure for a mature fault that has undergone slip localization within a shear band developed at the margin of a bulk gouge layer (Figure 6a). Frictional strength of the

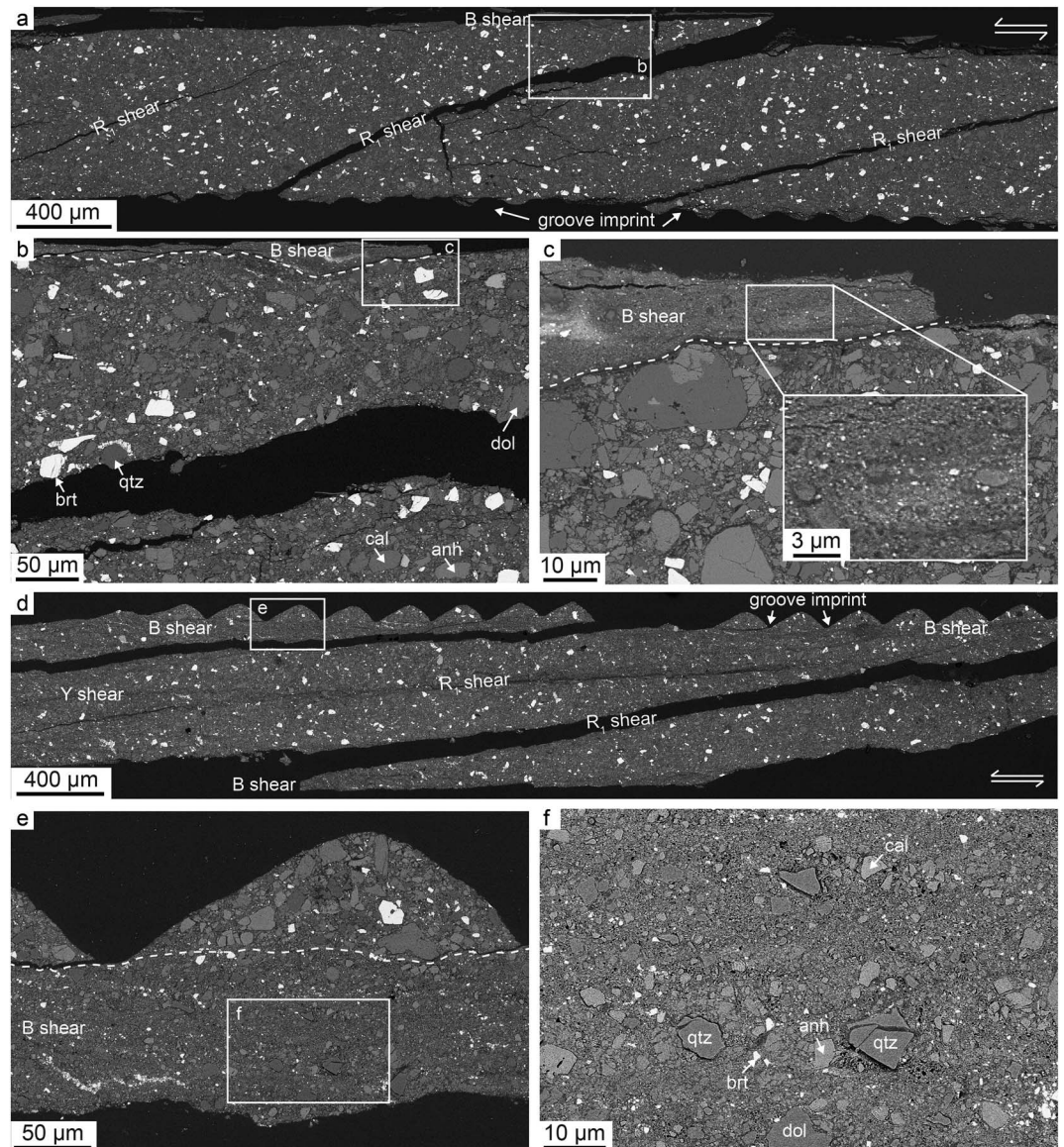


Figure 5. SEM BSE images showing representative microstructures exhibited by a brine-saturated sample (a–c, from experiment Z2BZ-06 tested at 100 °C) and an air-filled sample (d–f, from experiment Z2BZ-07 tested at 100 °C). The sense of shear is top-to-the-left in all images. (a) Part of the microstructure of Z2BZ-06, showing localization into a boundary shear and three R_1 Riedel shears. The groove/grip imprint from the porous driver block plate is preserved at the bottom of the sample. (b) Enlargement of the bulk gouge and boundary (B) shear band indicated at the top of Figure 5a. Mineral phases are indicated, from light to dark, as barite (brt), anhydrite (anh), dolomite (dol), calcite (cal), and quartz (qtz). (c) Detail of the boundary shear shown in Figure 5b, characterized by a marked reduction in grain size and a relatively dense fabric with clasts that are more rounded than in the bulk gouge (see inset showing a magnified image of the boundary shear band). Microfracturing and comminution are widely observed throughout the bulk gouge. (d) BSE image of a part of the microstructure of Z2BZ-07, showing localization into boundary shears at the top and bottom of the sample, plus two R_1 shears and a Y shear. The forcing block groove imprint is preserved at the top of the sample. (e and f) Details of the upper boundary shear in Figure 5d, showing a chaotic, granular microstructure with a relatively large proportion of relatively coarse grains in a matrix of grains that are smaller than 1 μm . Note that the porosity as seen in the boundary shear of the dry sample in Figure 5f appears to be higher than in the boundary shear of the wet sample in Figure 5c. SEM = scanning electron microscopy; BSE = backscattered electron.

fault gouge is assumed to be controlled by competition between two key mechanisms: (1) dilatant granular shear flow, with velocity-strengthening atomic-scale frictional interactions at sliding contacts, and (2) time-dependent shear and compaction by a thermally activated creep mechanism (e.g., pressure solution or

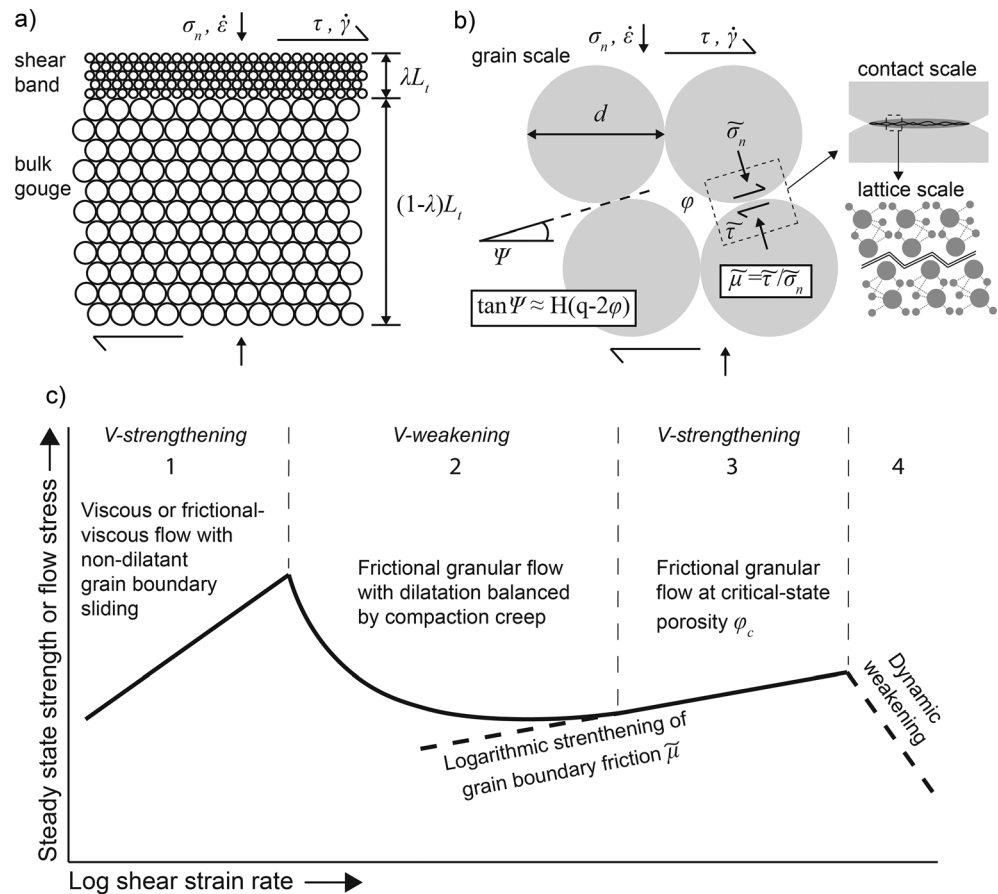


Figure 6. Overview of the CNS model adapted from Chen et al. (2017). (a) Conceptual model, showing bulk gouge and localized shear band with total thickness (L_t) and localization degree (λ). The applied normal stress (σ_n) and shear stress (τ) are associated with a fault-normal strain rate ($\dot{\epsilon}$) and shear strain rate ($\dot{\gamma}$). (b) Microstructural geometry assumed for bulk gouge and shear band with grain size (d), illustrating the grain contact angle (ψ) that is related to porosity (ϕ) via a geometrical parameter (H) and a parameter (q), defined as 2 times the critical state porosity for granular flow (ϕ_c). Deformation occurs by dilatant granular flow operating in competition with shear and normal deformation of the grains by a thermally activated creep process (e.g., pressure solution). The grain boundary friction coefficient ($\bar{\mu}$) is defined as the ratio of the local shear stress ($\bar{\tau}$) and normal stress ($\bar{\sigma}_n$) acting on the grain contacts and is described by atomic-scale barrier interactions, according to equation 5d in Table 2. At the contact scale (see inset), a single contact consists of many small-scale solid-solid islands or contact points. The inset at the lattice scale represent frictional sliding interactions of atoms at a single contact point, where large atoms represent anions and small atoms represent cations. (c) Qualitative sketch of steady state frictional strength versus shear strain rate following the CNS model, showing the flow regime (1) at low velocities, the frictional regimes (2 and 3) at intermediate velocities, and the dynamic weakening regime (4) at high velocities.

dislocation creep) acting at the grain scale (Figure 6b). A plot of steady state shear strength versus shear strain rate at constant temperature, as qualitatively predicted by the CNS model, is presented in Figure 6c following Chen et al. (2017). The model predicts velocity-strengthening behavior in the low strain rate regime due to nondilatant plastic/viscous flow. With increasing shear strain rate, dilatation sets in and the behavior transitions to velocity weakening. In this regime, frictional strength is controlled by the competition between shear-induced dilatation and time-dependent compaction, producing a steady state porosity and corresponding steady state strength at fixed shear rate. At higher shear rates still, critical state granular flow is approached, and velocity-strengthening behavior becomes dominant due to the velocity-strengthening nature of the grain boundary friction coefficient. At yet higher strain rates, dynamic slip- and/or velocity-weakening behavior is expected due to mechanisms activated by frictional heating (Aharonov & Scholz, 2018; Di Toro et al., 2011). The intermediate velocity-weakening/strengthening regimes (Regimes 2 and 3 in Figure 6c) are the most relevant for this paper.

Table 2
List of the Governing Equations, Input Parameters^a and Values Used in the Present CNS Model Simulations

Equation	Eq. No.	Conceptual meaning and source	
$\frac{\dot{\tau}}{K} = V_{\text{imp}} - L_t \dot{\gamma}_{\text{tot}} \& \dot{\gamma}_{\text{tot}} = (\dot{\gamma}_{\text{pl}} + \dot{\gamma}_{\text{gr}})$	5a	Fault-parallel kinematic relation (Chen & Spiers, 2016)	
$-\frac{\dot{\phi}}{(1-\phi)} = \dot{\epsilon}_{\text{pl}} - \dot{\gamma}_{\text{gr}} \tan\psi \& \tan\psi = H(q-2\phi)$	5b	Relation describing fault-normal deformation (Chen & Spiers, 2016)	
$\tau = \frac{\tilde{\mu} + \tan\psi}{1 - \tilde{\mu} \tan\psi} \sigma_n$	5c	Grain contact to REV scaling relation for friction coefficient (Chen & Spiers, 2016)	
$\tilde{\mu} = \tilde{\mu}^* + a_{\tilde{\mu}} \ln(\dot{\gamma}_{\text{gr}}/\dot{\gamma}_{\text{gr}}^*)$	5d	Grain contact friction equation (Chen & Spiers, 2016)	
$\dot{\epsilon}_{\text{pl}} = A_{\text{pl}} \frac{\sigma_n^p}{d^m} \exp\left(-\frac{E_a}{RT}\right) f_{\phi}$	6a	Creep law describing compaction rate at grain contacts (S2)	
$f_{\phi} = \left(1 - \frac{\phi}{\phi_c}\right)^{-M}$	6b	Porosity function accounting for changes in grain contact area (S2)	
Parameter	Description (unit)	Value (Range)	Source and additional information
τ	Shear stress (Pa)	Output from model	Equation 5c
σ_n	Effective normal stress (Pa)	4×10^7	Experimentally applied value
T	Absolute temperature (K)	323–423	Experimental applied values
K	Machine stiffness (Pa/m)	7×10^{10}	Calibrated value
V_{imp}	Imposed slip rate at load point (m/s)	$0.1 - 10 \times 10^{-6}$	Experimentally applied values
L_t	Thickness of the gouge layer (m)	8×10^{-4}	Observed from sheared samples
λ	Localization degree	0.02 (0.0125–0.0375)	Observed from sheared samples
ψ	Dilatation angle	Output from model	Equation 5b
ϕ	Porosity of the shear band	Output from model	Equation 5b
ϕ_c	Critical state porosity for granular flow	0.27	Assumed here
ϕ_0^{bulk}	Initial porosity of bulk gouge	0.25	Starting porosity in brine-saturated uniaxial compaction experiment (S1)
d	Average grain size of shear band (m)	0.5×10^{-6} ($0.1 - 2 \times 10^{-6}$)	Observed from microstructures
d^{bulk}	Average grain size of bulk gouge (m)	5×10^{-6} ($2 - 20 \times 10^{-6}$)	Observed from microstructures
q	2× critical state porosity	0.54	Empirically determined from compaction data (S2)
H	Geometrical parameter	0.577 (0.36–1.73)	Assumed here following Niemeijer and Spiers (2007)
$\tilde{\mu}^*$	Reference grain boundary friction coefficient for velocity of 1×10^{-6} m/s	0.65	Assumed here
$a_{\tilde{\mu}}$	Coefficient for logarithmic rate dependence of grain boundary friction	0.01 (0.002–0.06)	Experimentally determined from brine-sat. samples (av. a value from RSF fits)
$\sigma_n^p A_{\text{pl}}$	Temperature-independent constant in compaction creep law (m^3/s)	6.6×10^{-27}	Empirically determined value (S2)
E_a	Activation energy in compaction creep law (J/mol)	10×10^3 ($4 - 16 \times 10^3$)	Empirically determined value (Figure 4b)
R	Universal gas constant (J/mol/K)	8.314	Universal value
M	exponent in porosity function	4.8	Empirically determined value (S2)
m	Grain size sensitivity exponent in compaction creep law	3	Following Pluymakers and Spiers (2014)

^aOther symbols used are explained in the text.

4.2. CNS Model as Applied Here

As described above, the CNS model for truly frictional behavior of a fault gouge shear band (Regimes 2 and 3 of Figure 6c) assumes that gouge deformation involves parallel operation of dilatant granular flow and thermally activated (creep) deformation of individual grains. From a more quantitative perspective (refer Table 2), the gouge friction coefficient μ at any instant is determined by the gouge microstructure (porosity ϕ and dilatation angle ψ , Figure 6b) and by the grain contact friction coefficient $\tilde{\mu}$: see equations 5c and 5d (Table 2). Evolution of gouge porosity and dilatation angle is determined by competition between granular dilatation and compaction by the thermally activated creep process ($\dot{\epsilon}_{\text{pl}}$) according to equation 5b (Table 2), that is, by the net strain rate normal to the shear band. Similarly, the total shear band strain rate ($\dot{\gamma}_{\text{tot}}$ in equation 5a, see Table 2) is the sum of the shear rate due to granular flow ($\dot{\gamma}_{\text{gr}}$) plus that due to thermally activated

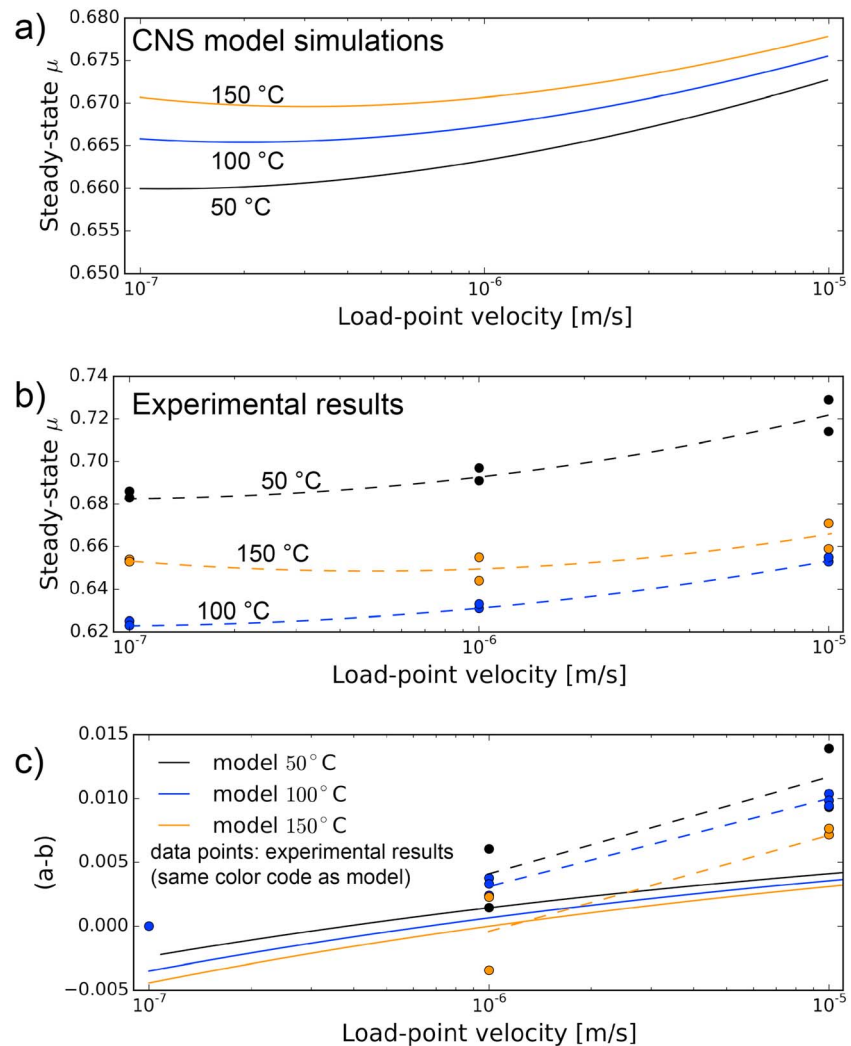


Figure 7. (a) Friction coefficient μ versus load-point velocity calculated from our CNS model simulations using the input parameters specified in Table 2. (b) μ versus load-point velocity data obtained in our brine-saturated samples (see Figure 2a), corrected for linear slip-weakening trends. Interpolated lines show general trends exhibited by the data. The simulations show trends in μ versus V at fixed temperature that are very similar to our experimental results, that is, a transition from velocity strengthening (positive slope) at 50 °C to velocity weakening (negative slope) at low velocities, at 150 °C (compare Figure 7a with 7b). However, the simulations show a continuous increase in μ with temperature at fixed velocity that is not seen in the experimental data. (c) $(a-b)$ calculated from the simulations (solid lines) and from experiments (data points plus interpolated lines) versus load-point velocity, showing similar trends versus velocity and temperature. CNS = Chen-Niemeijer-Spiers.

shear deformation ($\dot{\gamma}_{pl}$). Lastly, the load-point sliding velocity measured in an experiment can be represented by the sum of the gouge shearing velocity and the rate of elastic dimensional changes occurring in the shear loading system due to changes in shear stress supported by the active shear band (equation 5a, Table 2).

The CNS model as implemented by Chen and Spiers (2016) and Chen et al. (2017) solves this system of equations, also allowing for compaction of the bulk gouge (Figure 6a) without shear. Here we apply it for the observed microstructure in our brine-saturated experiments, using an empirical thermally activated compaction creep law given by equations 6a and 6b (Table 2) that was calibrated against independent compaction experiments (see supporting information, sections S1 and S2). Note that for the velocities investigated in this study (0.1–10 $\mu\text{m/s}$), shear deformation accommodated by creep ($\dot{\gamma}_{pl}$) is negligible, and we therefore neglected it in our simulations. The input parameters used in obtaining the steady state and transient

behavior in our CNS model simulations are listed in Table 2. For details on the final model implementation and solution method used the reader is referred to Chen and Spiers (2016) and Chen et al. (2017).

Regarding the mechanism of compaction operating in our basal Zechstein gouge, both our frictional and compaction results clearly point to a thermally activated mechanism, with low apparent activation energy for compaction in the bulk gouge, crudely estimated to be 10 ± 6 kJ/mol (Figure 4b). Uniaxial compaction experiments on solution-saturated monomineralic calcite and anhydrite aggregates under pressure and temperature conditions relevant here (Pluymakers & Spiers, 2014; Pluymakers, Peach, et al., 2014; Zhang et al., 2010) have shown that time-dependent compaction creep is controlled by intergranular pressure solution (IPS), giving way to subcritical crack growth control at grain sizes >70 μm . Based on these results, IPS is expected to dominate compaction in our brine-saturated experiments. Our estimate of the activation energy for bulk gouge compaction also agrees well with the range of values reported for calcite by Zhang et al. (2010, 6–24 kJ/mol), which are broadly consistent with diffusion-controlled IPS. Based on this, the grain size exponent (m) in the creep law (equation 6a, Table 2) was assumed to be 3 (Pluymakers & Spiers, 2014).

4.3. CNS Simulation Results Versus Experiments; Brine-Saturated Samples

To assess to what extent the CNS model can reproduce our experimental results quantitatively, we applied the model as described above, using the input parameters listed in Table 2 and simulating temperatures of 50, 100, and 150 °C. In Figures 7a and 7b we compare the steady state friction coefficient versus sliding velocity results obtained from these simulations with those measured in our brine-saturated experiments (corrected for linear background slip-weakening trends; cf. Blanpied et al., 1998). The corresponding (a - b) values determined from the simulations and the experiments are shown in Figure 7c. At individual temperatures, the simulations show trends in μ versus V that are closely similar to our experimental results, that is, positive slopes, hence velocity strengthening at 50 and 100 °C, transitioning to negative slopes, hence velocity weakening at 150 °C and velocities in the range 0.1–1 $\mu\text{m/s}$ (Figures 7a and 7b). Like the experimental data, the modeled (a - b) values also increase with velocity while decreasing with temperature (Figure 7c). In the CNS model, these trends represent the transition from Regime 2 to Regime 3 in Figure 6c, which occurs at increasingly higher rates as temperature increases due to more effective competition of thermally activated compaction versus granular dilation (the curve moves to the right in Figure 6c). A conspicuous shortcoming of the model, however, is that it predicts a continuous increase in μ with temperature at fixed velocity (again due to increasingly efficient compaction, hence lower φ), which is not seen in the experimental data where the frictional strength at 50 °C is greater than at 100 and 150 °C (Figure 7a vs 7b). It should be noted here that the uncertainty in friction coefficient related to experimental reproducibility is relatively large (± 0.02 , e.g., Hunfeld et al., 2017) compared to the variations in friction coefficient with temperature predicted by the model, and that at least part of this disparity may be related to this uncertainty.

In terms of transient behavior (Figure 8), the modeling results show a frictional strength response to velocity stepping that is closely similar to the experimental observations. For each velocity step, both the modeled and experimentally observed frictional strength first exhibits a direct effect and then evolves to a new steady state, consistent with velocity-strengthening behavior at 50 and 100 °C, and with partly unstable behavior (at 0.1 $\mu\text{m/s}$) at 150 °C. Moreover, at 150 °C and 0.1 $\mu\text{m/s}$, where the gouge is both observed and predicted to be velocity weakening (Figure 7), the model predicts unstable oscillations that decay with ongoing displacement, as observed in the experiment at 150 °C (though with higher frequency and lower amplitude). However, the experimental data show a peakless evolution toward steady state strength for fast upsteps (1–10 $\mu\text{m/s}$) that is characterized by an apparent negative b value (Figure 8 and Table S1), whereas the modeled friction shows a transient peak in frictional strength and hence positive b .

In summary, the CNS model qualitatively reproduces the main trends in μ versus velocity, and in (a - b) versus velocity and temperature, seen in our brine-saturated experiments, suggesting that the basic microstructural processes envisioned in the model (dilatant granular flow in combination with thermally activated compaction creep) may indeed control the frictional behavior seen in our experiments. However, there are aspects of the experimental data that are not captured at all in the modeling results. These are (i) the temperature dependence of μ at fixed velocity (Figure 7b versus 7a), (ii) the absence of a peak friction (negative b values) following fast upsteps (Figure 8), and (iii) the magnitude and recurrence time of the stick slips occurring at 150 °C and 0.1 $\mu\text{m/s}$, which are both overestimated in the modeling results (Figure 8c). Relevant here is the high sensitivity of the CNS model to microstructural parameters like grain size (d), porosity (φ) and shear band thickness (L_s), or

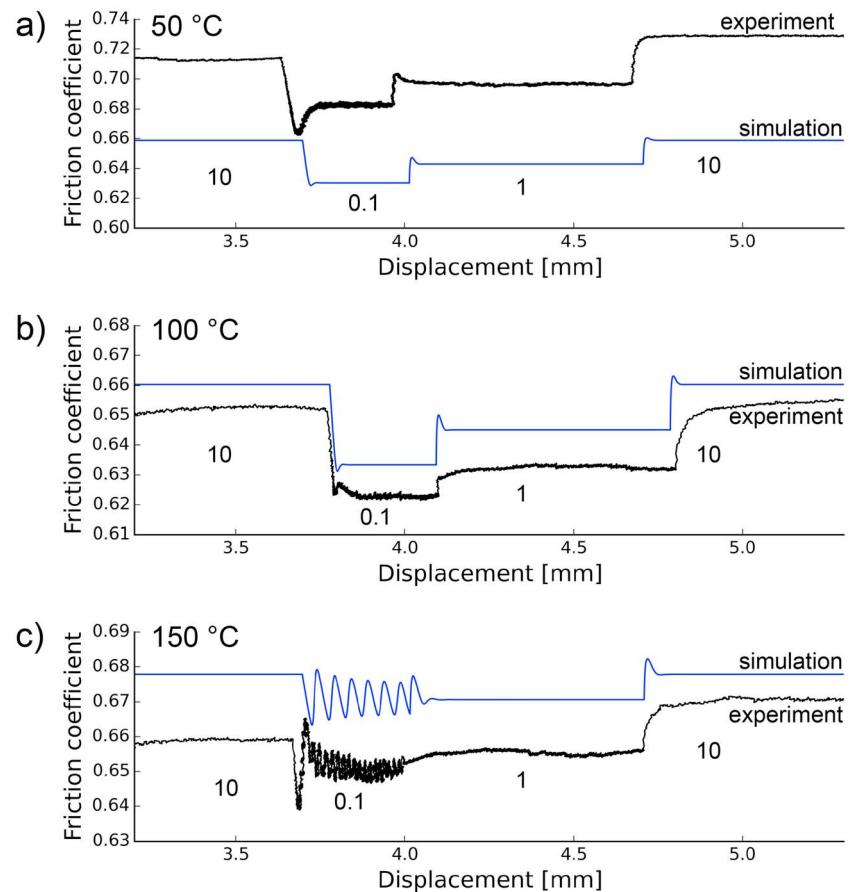


Figure 8. Friction coefficient μ versus displacement curves obtained in CNS model simulations (blue lines) and brine-saturated experiments (black lines, corrected for linear displacement-weakening trends) at (a) 50, (b) 100, and (c) 150 °C. The sliding velocities are as indicated per step in $\mu\text{m/s}$. The model simulations use the same values for the input parameters as the simulations in Figure 5, except for the following: for the 50 and 100 °C simulation, $\lambda = 0.0125$ (corresponding to a 10- μm wide shear band), and $H = 0.3$ (for comparison, these parameters were set, respectively, to 0.02 and 0.577 in Figure 5). For the 150 °C simulation, α_{μ} was set to be 0.009 instead of 0.01. These values were within the realistic ranges listed in Table 2. At all three temperatures, the simulations show a transient response in friction to velocity stepping that is similar to that seen in the experimental data, except for (1) the apparent negative b values that characterize the evolution toward steady state in steps of 1–10 $\mu\text{m/s}$ in the experiments, which is not captured in the simulations, and (2) the magnitude and recurrence time of the stick slips occurring at 0.1 $\mu\text{m/s}$ at 150 °C, which are both overestimated in the simulations. CNS = Chen-Niemeijer-Spiers.

localization degree (λ), as shown in Figure 9 [see also Chen & Spiers, 2016]. Variations in these parameters with temperature, for example, might account for the observed discrepancies in μ and stick-slip amplitude/frequency. Due to the fine grain size of the deformed samples, we have no microstructural evidence for such effects but cannot exclude them. Processes that affect localization (λ) and overall microstructure (d , φ), like grain-scale cataclasis and comminution, are not included in the model, though, based on our microstructures, they clearly played a role during deformation. To assess their effects, constant-velocity experiments to fixed strains should be performed in the future, with detailed microstructural analyses to gain insight into how grain size and localization degree develop during progressive shear and whether this development depends on sliding velocity. The apparent negative b observed in steps of 1–10 $\mu\text{m/s}$ (fast rates imposed) might reflect that the shear band porosity is at the critical state value, so that there is no dilatation in the shear band and thus no slip-weakening evolution effect.

4.4. Mechanisms Controlling Friction in Gas-Bearing and Evacuated Samples

The increase in friction from 0.64 to 0.72 ± 0.02 observed in our experiments on gas-filled/evacuated samples at 100 °C compared to brine-saturated experiments at the same temperature (Figure 2) can potentially be

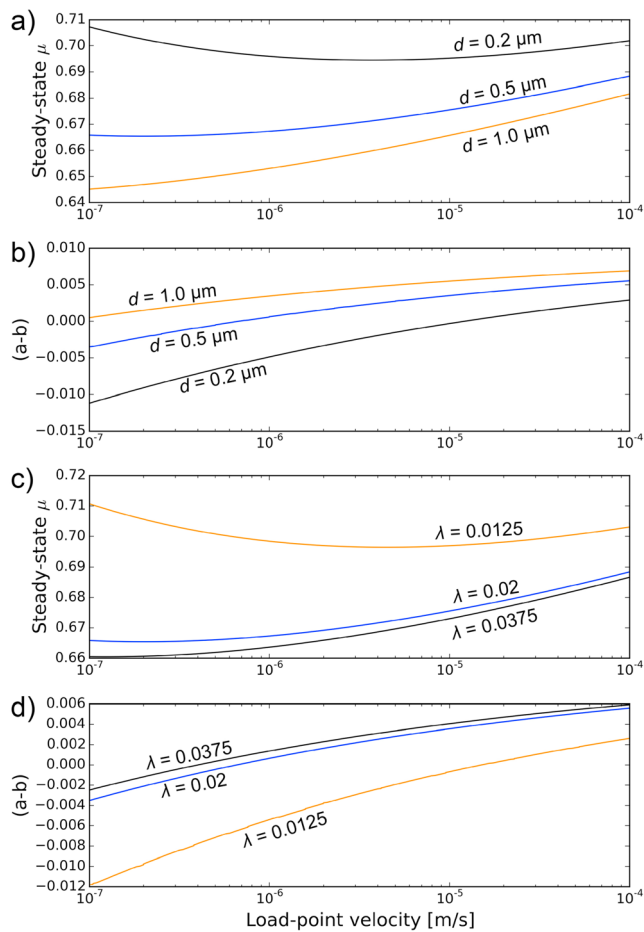


Figure 9. CNS model results in terms of friction coefficient μ and (a-b) versus load-point velocity at 100 °C, showing the sensitivity to grain size d (a and b) and degree of shear localization λ (c and d). The values for d and λ were varied within realistic ranges (see Table 2). The values for the other parameters were equal to the reference-case scenario in Table 2. For comparison, the green curves in Figures 9a and 9b (using $d = 0.5 \mu\text{m}$ and $\lambda = 0.0125$) correspond to the 100 °C simulations shown in Figures 5a and 5c. For an overview of the sensitivity of the CNS model to other input parameters, the reader is referred to Chen and Spiers (2016). CNS = Chen-Niemeijer-Spiers.

explained by the effects of water on intergranular friction ($\bar{\mu}$). Lubrication by adsorbed (disjoining) water films has frequently been proposed to reduce sliding friction between grains (e.g., Morrow et al., 2000) through viscous layer effects or through surface force interactions that reduce atomic scale barriers to intergranular slip or else remove them by local diffusive transport (Diao & Espinosa-Marzal, 2018, refer Figure 6b). Hence, grain boundary and aggregate friction are expected to be higher in samples that do not contain aqueous pore fluids. On the other hand, our partially saturated gouges showed friction coefficients comparable to dry gouges, suggesting that molecular water films adsorbed at grain boundaries were either not sufficiently thick to reduce friction or that sorption sites were not sufficiently populated or occupied at all (no films present). A possible explanation behind this lies in the distribution of the aqueous fluid under mixed gas-brine conditions (Jiang et al., 2013). Grain contacts in our partially saturated gouges may have been preferentially saturated with adsorbed gas molecules (gas wetted), with liquid water being present only as isolated brine droplets in the free pores, thus leading to high, near-dry friction coefficients. To the best of our knowledge, however, no data are available on sorption or wetting of materials such as the present gouge, by either N_2 /brine or CH_4 /brine mixtures, to evaluate this hypothesis.

We now attempt to explain the velocity-weakening behavior observed in our gas-bearing, gas/brine-bearing, and evacuated gouge samples at 100 °C, recalling that brine-saturated samples showed velocity strengthening at this temperature (Figure 3). In the CNS model, velocity weakening is expected when the rate of compaction creep competes with the rate of dilatation caused by granular flow. Zhang et al. (2010) and Pluymakers, Peach, et al. (2014) showed that under (vacuum) dry conditions, compaction creep in granular calcite and anhydrite aggregates is dominated by subcritical cracking at the grain scale, possibly aided by minor, work-hardening crystal plasticity (dislocation glide), and occurs at rapidly decelerating rates reaching values far lower than seen under wet (fluid-saturated) conditions at porosities below 30%. We confirmed similar behavior in uniaxial compaction experiments on vacuum-dry basal Zechstein samples. These too showed rapidly decelerating compaction that reached negligible rates compared with brine-saturated material at porosities below ~31% (see supporting information section S1). The rate of compaction of partially saturated basal Zechstein gouge (tested at 100 °C using air plus brine, see supporting information section S1) at these porosities was also orders of magnitude lower than for brine-saturated material and showed a similarly rapid decrease in strain rate with porosity to the vacuum-dry samples, suggesting a similar compaction mechanism.

This slow compaction creep in dry and partially saturated gouge samples should promote critical state, velocity-strengthening behavior (Regime 3, Figure 6c), rather than the observed velocity weakening, at rapid shear rates, because compaction creep would be unable to compete with dilatation due to granular flow. On the other hand, the higher porosities (~20–30%) observed in our sheared gas-bearing and evacuated samples compared to wet samples (~10–20%) imply higher stresses at grain contacts. These in turn imply potentially higher compaction rates during steady state shearing of the dry and partially saturated samples since the strain rate due to subcritical microcracking and dislocation glide processes inferred in dry anhydrite and calcite gouges (Pluymakers, Peach, et al., 2014; Zhang et al., 2010) depends exponentially on grain contact stress, as opposed to the linear dependence characteristic of pressure solution (De Bresser, 2002; Munz & Fett, 1999; Rybacki et al., 2013; Spiers et al., 2004).

Combined with dilatant granular flow plus an increased grain boundary friction coefficient under (partially) dry conditions, shear and compaction creep by the above-mentioned subcritical cracking and dislocation

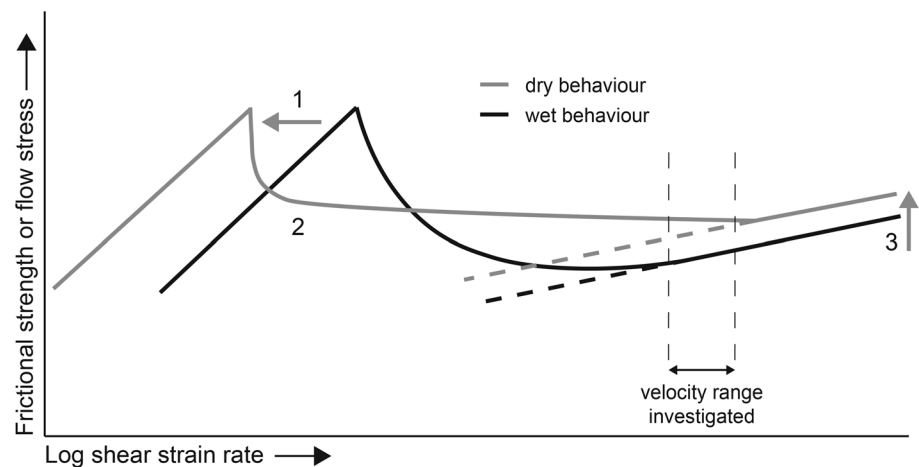


Figure 10. Schematic illustration showing the proposed explanation for the results of experiments on gas-bearing and evacuated samples. Under these conditions, the steady state frictional strength versus shear strain rate curve for wet behavior as predicted by the CNS model (black line; see also Figure 1c) is altered as follows: (1) the switch from shear and compaction creep by pressure solution in wet samples to subcritical cracking or dislocation mechanisms in (partially) dry samples shifts velocity-strengthening ductile behavior and the onset of velocity-weakening behavior to lower velocities; (2) the lower rate of compaction under (partially) dry conditions at a given developing porosity and the increased sensitivity of dry compaction mechanisms to contact stresses and changing porosity changes the shape of the curve in the velocity-weakening regime (see main text for discussion), resulting in a steeper curve at low velocities, and more linear (but still velocity weakening) toward higher velocities where the transition to critical state granular flow with velocity-strengthening (dry) grain boundary friction ultimately occurs; (3) the increased (dry) grain boundary friction coefficient shifts the frictional strength in the granular flow regime to higher values. These combined effects can potentially explain the velocity-weakening behavior observed for gas-bearing and evacuated gouges in the range of sliding velocities investigated in our experiments. CNS = Chen-Niemeijer-Spiers.

mechanisms could potentially produce the steady state friction versus velocity behavior for dry material shown in Figure 10—according to the principles of the CNS model. In Figure 10, velocity strengthening ductile behavior and the onset of the dilatant velocity-weakening regime are shifted toward lower velocities in the case of (partially) dry samples, due to a switch to shear and compaction creep by subcritical cracking or dislocation glide mechanisms, as opposed to faster pressure solution in the fully wet samples. At the same time, the shape of the curve in the velocity-weakening region, where porosity develops due to a balance between dilatation associated with granular flow versus compaction creep, is altered due to (a) the lower rate of compaction under (partially) dry conditions at a given developing porosity and (b) the increased sensitivity of dry compaction mechanisms to contact stress and to changing porosity. The velocity-weakening curve for the (partially) dry case is thus steepened at low velocities because sluggish compaction allows rapid dilatation and hence a rapid shear strength drop until the porosity is high enough for compaction by subcritical cracking or dislocation mechanisms to match the dilatation rate. Continued velocity weakening toward higher velocities then proceeds much more gradually (more linearly) as the background porosity level is now high enough for continued dilatation to be matched by small increases in compaction rate as grain contact areas decrease and contact stresses increase. As the transition to critical-state granular flow is approached (i.e., when dilatant granular flow is so fast that compaction by subcritical cracking or dislocation mechanisms is negligible) then velocity-strengthening sets in due to the influence of velocity strengthening (dry) grain boundary friction.

We postulate that this combination of increased grain boundary friction plus highly stress-sensitive compaction mechanism offers an explanation for the increased frictional strength and the velocity-weakening behavior observed in our dry and partially saturated samples versus the brine-saturated. However, if we consider that the creep mechanism is stress-corrosion cracking, this implies that grain size is continuously evolving during the experiments, which violates the assumption of a steady state microstructure in the CNS model. Besides a change in grain size, the continuous operation of grain size reduction might also affect the development of the width of the localized shear band(s). In this context, it is interesting to note that we observe a continuous strain weakening in the gas-bearing samples that appears to be absent in the wet samples (at

100 °C at least; Figure 2b). This could potentially be related to a decrease in the intensity of grain size reduction. A final possibility that we consider is the nature of the velocity dependence of grain boundary friction. If this were to be velocity weakening in the absence of an aqueous pore fluid, it could also explain the behavior observed in our experiments. However, to the best of our knowledge, there is no mechanistic basis that supports this. The atomic- to nanometer-scale interactions at grain contacts considered in the CNS model produce velocity-strengthening behavior (Chen & Spiers, 2016), as does any thermally activated atomic or defect scale barrier jump process at asperity contacts (Beeler et al., 1996; Diao & Espinosa-Marzal, 2018; Nakatani, 2001; Rice et al., 2001; Tullis & Weeks, 1987).

4.5. Implications

The results presented in this study show that the frictional properties of simulated basal Zechstein fault gouges are highly sensitive to temperature and pore fluid conditions. Besides direct implications for induced seismicity in the Groningen gas field, the results are also relevant to induced and natural seismicity related to faults cutting anhydrite- and carbonate-dominated sequences worldwide.

In the Groningen gas field, the top of the reservoir system, that is, the Slochteren sandstone and overlying Ten Boer claystone, is saturated mainly with gas (mostly methane with ~14 % nitrogen (De Jager & Visser, 2017; Stauble & Milius, 1970)) alongside connate brine (the connate water content in the reservoir varies between 7-25 % (Burkitov et al., 2016)). Faults that cut through the basal Zechstein and into the reservoir (including those that juxtapose the reservoir against the overlying basal Zechstein caprock and thus incorporate anhydrite and carbonate gouges derived from the caprock) are therefore expected to be saturated with a mixture of CH₄ and brine. Our results for (*a-b*) in gas/brine-bearing samples (Figure 3c) show that under these conditions, faults containing basal Zechstein-derived gouge material are expected to be strongly velocity weakening. Coupled with their high friction coefficient, such faults would therefore be expected to be especially prone to the nucleation of seismogenic slip, in the framework of RSF. By comparison, the other formations in the reservoir system (i.e., the Ten Boer claystone, Slochteren sandstone, and Carboniferous shales/siltstone substrate) were found to be velocity strengthening (Hunfeld et al., 2017) and hence are not earthquake prone. However, there is little evidence from earthquake hypocenter estimations that supports this. Spetzler and Dost (2017) found that the majority of the events occur in the reservoir interval, with only ~5 to at most 30% of the events occurring in the upper part of the reservoir/caprock system. Relevant here is that other factors besides velocity weakening may influence fault reactivation and earthquake nucleation sites, such as a nonuniform stress distribution on faults due to the response of juxtaposed mechanically contrasting layers to reservoir depletion (Buijze et al., 2015; Mulders, 2003) or stress redistribution due to the presence of viscoelastic rock salt overlaying the basal Zechstein (Orlic & Wassing, 2012; Wassing et al., 2017). The fact that earthquakes are not uniquely associated with the upper part of the reservoir/caprock system may indicate that faults that cut this part of the system and incorporate basal Zechstein-derived gouge material are not critically stressed. Another possibility is that other mechanical behavior, such as slip weakening, plays a role in earthquake nucleation in the reservoir interval. The potential for this type of behavior needs to be addressed in future studies.

In contrast to gas-bearing gouges, our results show velocity-strengthening behavior under brine-saturated conditions at temperatures lower than or equal to the reservoir temperature in the Groningen field (~100 °C), implying stable, aseismic slip under such conditions. However, as pointed out by Hunfeld et al. (2017), the positive dependence of (*a-b*) on sliding velocity observed in brine-saturated basal Zechstein gouges implies that at lower displacement rates, velocity-weakening behavior occurs, which can potentially initiate accelerating slip. For temperatures above 100 °C and under natural loading conditions, basal Zechstein gouge and anhydrite- and carbonate-dominated gouges in general are expected to produce velocity-weakening behavior, consistent with the laboratory results referenced earlier. This transition appears to correspond to the upper limit of the seismogenic zone in tectonically active evaporite and limestone terrains, located at ~2- to 4-km depth in the Apennines and the Corinth rift zone, for example (Bernard et al., 2006; Valoroso et al., 2013).

The CNS model seems to partially capture the experimentally observed temperature-dependent transition in slip stability, including the steady state and transient behavior exhibited in our brine-saturated experiments. As such, the CNS model and microphysically based models in general offer a promising tool for further quantification and understanding of the frictional properties of fault gouges under hydrothermal

conditions and to extrapolate laboratory results to pressures, temperatures, and sliding velocities outside laboratory capabilities. Our application of the CNS model here provides evidence that the velocity dependence of friction seen in the Basal Zechstein gouges studied is caused by the operation of dilatant granular flow in combination with either thermally activated compaction creep (likely diffusion-controlled IPS) in the case of brine-saturated gouges or highly stress-sensitive compaction mechanisms like subcritical crack growth and work-hardening crystal plasticity in the case of gas-bearing, partially saturated or dry gouges.

5. Conclusions

We performed direct shear, velocity-stepping friction experiments on simulated anhydrite-carbonate fault gouges prepared from the basal Zechstein caprock overlying the seismogenic Groningen gas field. We investigated its frictional properties at in situ P - T conditions, at temperatures of 50–150 °C, and at 40-MPa effective normal stress, using sliding velocities of 0.1–10 $\mu\text{m/s}$. We simulated the in situ pore fluid conditions using 4.4 M NaCl solution, as well as methane, air, and brine/gas mixtures. The results were analyzed in the classical RSF framework, as well as using a microphysical model for fault gouge friction. Our main findings are summarized below:

1. Brine-saturated basal Zechstein gouges showed steady state friction coefficients (μ) of 0.60–0.69, with little dependence temperature, along with velocity-strengthening behavior at 50–100 °C transitioning to velocity weakening at 120 °C and above.
2. Samples saturated with methane/air or gas-brine mixtures, as well as a vacuum-dry control experiment, showed μ values of 0.72 ± 0.02 plus strongly velocity-weakening behavior accompanied by stick slip at 100 °C (the only temperature investigated).
3. Microstructures of brine-saturated samples showed strongly localized shear in Riedel and boundary shear bands, characterized by extreme grain size reduction. Gas-filled, evacuated, and partially saturated samples showed similar microstructures, but with much wider shear bands that showed less extreme grain size reduction, and overall higher porosity as seen in our micrographs.
4. A microphysical model for friction of granular fault gouges (Chen et al., 2017; Chen & Spiers, 2016), assuming competition between dilatant granular flow and thermally activated compaction creep, captures most of the trends seen in our brine-saturated samples when applied using compaction creep data measured for simulated gouge that is assumed to reflect diffusion-controlled pressure solution. The behavior observed in our gas-bearing and dry samples can be qualitatively explained by the model assuming compaction creep due to stress-sensitive mechanisms such as subcritical crack growth and work-hardening crystal plasticity.
5. Noting that the temperature in the Groningen reservoir is ~ 100 °C, our results imply that faults crosscutting the basal Zechstein caprock and juxtaposing the caprock against the reservoir sandstone may show strong velocity-weakening behavior, specifically in the gas-filled upper portion of the reservoir/caprock system. From a RSF point of view, these faults thus have an increased potential for nucleating seismogenic slip in comparison with the underlying formations. Under brine-saturated conditions, velocity weakening and hence seismogenesis are expected at temperatures of 120 °C and above, which is relevant for natural seismicity occurring in evaporite and limestone terrains.

Acknowledgments

This research was funded by the Nederlandse Aardolie Maatschappij (NAM). The technical staff of the HPT Laboratory at Utrecht University are thanked for their assistance, specifically Gert Kastelein, Floris van Oort, and Peter van Krieken. Leonard Bik is thanked for preparing the sections. We thank Chris Marone and an anonymous reviewer for their constructive comments that helped improve this manuscript. J. Chen was in part funded by European Research Council starting grant SEISMIC (335915). A. R. Niemeijer was funded by SEISMIC (335915) and by the Netherlands Organization for Scientific Research (NWO) through VIDI grant 854.12.011. The data for this paper are available as Hunfeld et al. (2019): Friction and compaction data from simulated fault gouges derived from the basal Zechstein caprock of the Groningen gas field. <https://public.yoda.uu.nl/geo/UU01/PL06JQ.html> DOI: 10.24416/UU01-PL06JQ

References

- Aharonov, E., & Scholz, C. H. (2018). A physics-based rock friction constitutive law: Steady state friction. *Journal of Geophysical Research: Solid Earth*, 123, 1591–1614. <https://doi.org/10.1002/2016JB013829>
- Alsharhan, A. S., & Nairn, A. E. M. (1994). The late Permian carbonates (Khuff Formation) in the western Arabian Gulf: Its hydrocarbon parameters and paleogeographical aspects. *Carbonates and Evaporites*, 9(2), 132–142. <https://doi.org/10.1007/BF03175226>
- Andrews, D. J. (1976). Rupture Propagation With Finite Stress in Antiplane Strain. *Journal of Geophysical Research*, 81(20), 3575–3582. <https://doi.org/10.1029/JB081i020p03575>
- Beeler, N. M., Tullis, T. E., Blanpied, M. L., & Weeks, J. D. (1996). Frictional behavior of large displacement experimental faults. *Journal of Geophysical Research*, 101(B4), 8697–8715. <https://doi.org/10.1029/96JB00411>
- Bernard, P., Lyon-Caen, H., Briole, P., Deschamps, A., Boudin, F., Makropoulos, K., et al. (2006). Seismicity, deformation and seismic hazard in the western rift of Corinth: New insights from the Corinth Rift Laboratory (CRL). *Tectonophysics*, 426(1–2), 7–30. <https://doi.org/10.1016/j.tecto.2006.02.012>
- Blanpied, M. L., Lockner, D. A., & Byerlee, J. D. (1995). Frictional slip of granite at hydrothermal conditions. *Journal of Geophysical Research*, 100(B7), 13045. <https://doi.org/10.1029/95JB00862>

- Blanpied, M. L., Marone, C. J., Lockner, D. A., Byerlee, J. D., & King, D. P. (1998). Quantitative measure of the variation in fault rheology due to fluid-rock interactions. *Journal of Geophysical Research*, *103*(B5), 9691. <https://doi.org/10.1029/98JB00162>
- Boulton, C., Moore, D. E., Lockner, D. A., Toy, V. G., Townend, J., & Sutherland, R. (2014). Frictional properties of exhumed fault gouges in DFDP-1 cores, Alpine Fault, New Zealand. *Geophysical Research Letters*, *41*, 356–362. <https://doi.org/10.1002/2013GL058236>. Received
- Buijze, L., Orlic, B., & Wassing, B. B. T. (2015). Modeling of dynamic fault rupture in a depleting gas field, TNO report 2015 R10844.
- Burkitov, U., Van Oeveren, H., & Valvatne, P. (2016). Groningen Field Review 2015 Subsurface Dynamic Modelling Report.
- Byerlee, J. (1978). Friction of rocks. *Pure and Applied Geophysics PAGEOPH*, *116*(4–5), 615–626. <https://doi.org/10.1007/BF00876528>
- Carpenter, B. M., Colletini, C., Viti, C., & Cavallo, A. (2016). The influence of normal stress and sliding velocity on the frictional behaviour of calcite at room temperature: Insights from laboratory experiments and microstructural observations. *Geophysical Journal International*, *205*, 548–561. <https://doi.org/10.1093/gji/ggw038>
- Chen, J., Niemeijer, A. R., & Spiers, C. J. (2017). Microphysically derived expressions for rate-and-state friction parameters, a , b , and Dc . *Journal of Geophysical Research: Solid Earth*, *122*, 9627–9657. <https://doi.org/10.1002/2017JB014226>
- Chen, J., & Spiers, C. J. (2016). Rate and state frictional and healing behavior of carbonate fault gouge explained using microphysical model. *Journal of Geophysical Research: Solid Earth*, *121*, 8642–8665. <https://doi.org/10.1002/2016JB013470>
- Chen, J., Verberne, B. A., & Spiers, C. J. (2015). Effects of healing on the seismic potential of carbonate fault rocks: Experiments on samples from the Longmenshan fault, Sichuan, China. *Journal of Geophysical Research: Solid Earth*, *120*, 5479–5506. <https://doi.org/10.1002/2014JB011859>
- Chester, F. M. (1994). Effects of temperature on friction: constitutive equations and experiments with quartz gouge. *Journal of Geophysical Research*, *99*(B4), 7247–7261. <https://doi.org/10.1029/93JB03110>
- Colletini, C., De Paola, N., & Faulkner, D. R. (2009). Insights on the geometry and mechanics of the Umbria-Marche earthquakes (Central Italy) from the integration of field and laboratory data. *Tectonophysics*, *476*(1–2), 99–109. <https://doi.org/10.1016/j.tecto.2008.08.013>
- De Bresser, J. H. P. (2002). On the mechanism of dislocation creep of calcite at high temperature: Inferences from experimentally measured pressure sensitivity and strain rate sensitivity of flow stress. *Journal of Geophysical Research*, *107*(B12), 2337. <https://doi.org/10.1029/2002JB001812>
- De Jager, J., & Geluk, M. C. (2007). Petroleum geology. In *Geology of the Netherlands* (pp. 241–264). Amsterdam: Royal Netherlands Academy of Arts and Sciences.
- De Jager, J., & Visser, C. (2017). Geology of the Groningen field—An overview. *Netherlands Journal of Geosciences*, *95*(5), 3–15. <https://doi.org/10.1017/njg.2017.22>
- De Paola, N., Colletini, C., Faulkner, D. R., & Trippetta, F. (2008). Fault zone architecture and deformation processes within evaporitic rocks in the upper crust. *Tectonics*, *27*, TC4017. <https://doi.org/10.1029/2007TC002230>
- den Hartog, S. A. M., & Spiers, C. J. (2013). Influence of subduction zone conditions and gouge composition on frictional slip stability of megathrust faults. *Tectonophysics*, *600*, 75–90. <https://doi.org/10.1016/j.tecto.2012.11.006>
- den Hartog, S. A. M., & Spiers, C. J. (2014). A microphysical model for fault gouge friction applied to subduction megathrusts. *Journal of Geophysical Research: Solid Earth*, *119*, 1510–1529. <https://doi.org/10.1002/2014JB011151>
- Di Toro, G., Han, R., Hirose, T., De Paola, N., Nielsen, S., Mizoguchi, K., et al. (2011). Fault lubrication during earthquakes. *Nature*, *471*(7339), 494–498. <https://doi.org/10.1038/nature09838>
- Diao, Y., & Espinosa-Marzal, R. M. (2018). The role of water in fault lubrication. *Nature Communications*, *9*(1). <https://doi.org/10.1038/s41467-018-04782-9>
- Dieterich, J. H. (1978). Preseismic fault slip and earthquake prediction. *Journal of Geophysical Research*, *83*(B8), 3940. <https://doi.org/10.1029/JB083iB08p03940>
- Dieterich, J. H. (1979). Modeling of rock friction: 1. Experimental results and constitutive equations. *Journal of Geophysical Research*, *84*(9), 2161–2168.
- Dieterich, J. H. (1994). A constitutive law for rate of earthquake production and its application to earthquake clustering. *Journal of Geophysical Research*, *99*, 2601–2601.
- Geluk, M. C. (2007). Permian. In T. E. Wong, D. A. J. Batjes, & J. De Jager (Eds.), *Geology of the Netherlands* (p. 63–83). Amsterdam: Royal Netherlands Academy of Arts and Sciences.
- Hunfeld, L., Chen, J., Niemeijer, A., & Spiers, C. (2019). Friction and compaction data of simulated fault gouges derived from the Basal Zechstein caprock of the Groningen gas field. <https://public.yoda.uu.nl/geo/UU01/PL06JQ.html>. <https://doi.org/10.24416/UU01-PL06JQ>
- Hunfeld, L. B., Niemeijer, A. R., & Spiers, C. J. (2017). Frictional properties of simulated fault gouges from the seismogenic Groningen gas field under in-situ P-T-chemical conditions. *Journal of Geophysical Research: Solid Earth*, *122*, 8969–8989. <https://doi.org/10.1002/2017JB014876>
- Ida, Y. (1972). Cohesive force across the tip of a longitudinal-shear crack and Griffith's specific surface energy. *Journal of Geophysical Research*, *77*(20), 3796–3805. <https://doi.org/10.1029/JB077i020p03796>
- Ikari, M. J., Carpenter, B. M., & Marone, C. (2016). A microphysical interpretation of rate- and state-dependent friction for fault gouge. *Geochemistry, Geophysics, Geosystems*, *17*, 1–18. <https://doi.org/10.1002/2016GC006286>
- Ikari, M. J., Saffer, D. M., & Marone, C. (2009). Frictional and hydrologic properties of clay-rich fault gouge. *Journal of Geophysical Research*, *114*, B05409. <https://doi.org/10.1029/2008JB006089>
- Jiang, G., Li, Y., & Zhang, M. (2013). Evaluation of gas wettability and its effects on fluid distribution and fluid flow in porous media. *Petroleum Science*, *10*(4), 515–527. <https://doi.org/10.1007/s12182-013-0303-4>
- Kato, N., & Tullis, T. E. (2003). Numerical simulation of seismic cycles with a composite rate- and state-dependent friction law. *Bulletin of the Seismological Society of America*, *93*(2), 841–853. <https://doi.org/10.1785/0120020118>
- Logan, J. M., Friedman, M., Higgs, N., Dengo, C., & Shimamoto, T. (1979). Experimental studies of simulated gouge and their application to studies of natural fault zones, *US Geol. Surv. Open-File Rep.*, 79–1239.
- Marone, C. J. (1998). Laboratory-derived friction laws and their application to seismic faulting. *Annual Review of Earth and Planetary Sciences*, *26*(1), 643–696. <https://doi.org/10.1146/annurev.earth.26.1.643>
- Morrow, C. A., Moore, D. E., & Lockner, D. A. (2000). The effect of mineral bond strength and adsorbed water on fault gouge frictional strength. *Geophysical Research Letters*, *27*(6), 815–818. <https://doi.org/10.1029/1999GL008401>
- Mulders, F. M. M. (2003). *Modelling of stress development and fault slip in and around a producing gas reservoir*. Delft, Netherlands: Delft University of Technology.

- Munz, D., & Fett, T. (1999). Subcritical crack growth. In *Ceramics: Mechanical properties, failure behavior, materials selection* (1st ed., pp. 77–108). Berlin Heidelberg: Springer-Verlag.
- Nakatani, M. (2001). Conceptual and physical clarification of rate and state friction: Frictional sliding as a thermally activated rheology. *Journal of Geophysical Research*, *106*(B7), 13,347–13,380. <https://doi.org/10.1029/2000JB900453>
- Niemeijer, A. R., & Spiers, C. J. (2006). Velocity dependence of strength and healing behaviour in simulated phyllosilicate-bearing fault gouge. *Tectonophysics*, *427*(1–4), 231–253. <https://doi.org/10.1016/j.tecto.2006.03.048>
- Niemeijer, A. R., & Spiers, C. J. (2007). A microphysical model for strong velocity weakening in phyllosilicate-bearing fault gouges. *Journal of Geophysical Research*, *112*, B10405. <https://doi.org/10.1029/2007JB005008>
- Orlic, B., & Wassing, B. B. T. (2012). Modeling stress development and fault slip in producing hydrocarbon reservoirs overlain by rock salt caprocks. In *46th US Rock Mechanics/Geomechanics Symposium*. American Rock Mechanics Association.
- Pluymakers, A. M. H., Niemeijer, A. R., & Spiers, C. J. (2016). Frictional properties of simulated anhydrite/dolomite fault gouge: Implications for seismogenic potential. *Journal of Structural Geology*, *84*, 31–46. <https://doi.org/10.1016/j.jsg.2015.11.008>
- Pluymakers, A. M. H., Peach, C. J., & Spiers, C. J. (2014). Diagenetic compaction experiments on simulated anhydrite fault gouge under static conditions. *Journal of Geophysical Research: Solid Earth*, *119*, 4123–4148. <https://doi.org/10.1002/2014JB011073>
- Pluymakers, A. M. H., Samuelson, J. E., Niemeijer, A. R., & Spiers, C. J. (2014). Effects of temperature and CO₂ on the frictional behavior of simulated anhydrite fault rock. *Journal of Geophysical Research: Solid Earth*, *119*, 8728–8747. <https://doi.org/10.1002/2014JB011575>
- Pluymakers, A. M. H., & Spiers, C. J. (2014). Compaction creep of simulated anhydrite fault gouge by pressure solution: Theory vs. experiments and implications for fault sealing. *Geological Society of London, Special Publication*, *409*. <https://doi.org/10.1144/SP409.6>
- Rice, J. R., Lapusta, N., & Ranjith, K. (2001). Rate and state dependent friction and the stability of sliding between elastically deformable solids. *Journal of the Mechanics and Physics of Solids*, *49*(9), 1865–1898. [https://doi.org/10.1016/S0022-5096\(01\)00042-4](https://doi.org/10.1016/S0022-5096(01)00042-4)
- Ruina, A. (1983). Slip instability and state variable friction laws. *Journal of Geophysical Research*, *88*, 10,359–10,370.
- Rybacki, E., Evans, B., Janssen, C., Wirth, R., & Dresen, G. (2013). Influence of stress, temperature, and strain on calcite twins constrained by deformation experiments. *Tectonophysics*, *601*, 20–36. <https://doi.org/10.1016/j.tecto.2013.04.021>
- Samuelson, J., & Spiers, C. J. (2012). Fault friction and slip stability not affected by CO₂ storage: Evidence from short-term laboratory experiments on North Sea reservoir sandstones and caprocks. *International Journal of Greenhouse Gas Control*, *11*, S78–S90. <https://doi.org/10.1016/j.ijggc.2012.09.018>
- Scholz, C. H. (2002). *The mechanics of earthquakes and faulting* (2nd ed.). Cambridge: Cambridge University Press.
- Scuderi, M. M., Niemeijer, A. R., Collettini, C., & Marone, C. (2013). Frictional properties and slip stability of active faults within carbonate–evaporite sequences: The role of dolomite and anhydrite. *Earth and Planetary Science Letters*, *369–370*, 220–232. <https://doi.org/10.1016/j.epsl.2013.03.024>
- Segall, P. (1989). Earthquakes triggered by fluid extraction. *Geology*, *17*(10), 942–946. [https://doi.org/10.1130/0091-7613\(1989\)017<0942:ETBFE>2.3.CO](https://doi.org/10.1130/0091-7613(1989)017<0942:ETBFE>2.3.CO)
- Shimamoto, T. (1986). Transition between frictional slip and ductile flow for halite shear zones at room temperature. *Science*, *231*(4739), 711–714. <https://doi.org/10.1126/science.231.4739.711>
- Sibson, R. H. (1986). Earthquakes and rock deformation in crustal fault zones. *Annual Review of Earth and Planetary Sciences*, *14*, 149–175.
- Speranza, F., & Minelli, L. (2014). Ultra-thick Triassic dolomites control the rupture behavior of the central Apennine seismicity: Evidence from magnetic modeling of the L'Aquila fault zone. *Journal of Geophysical Research: Solid Earth*, *119*, 6756–6770. <https://doi.org/10.1002/2014JB011199>
- Spetzler, J., & Dost, B. (2017). Hypocenter estimation of induced earthquakes in Groningen. *Geophysical Journal International*, *209*(1), 453–465.
- Spiers, C. J., De Meer, S., Niemeijer, A. R., & Zhang, X. (2004). Kinetics of rock deformation by pressure solution and the role of thin aqueous films. In S. Nakashima, C. J. Spiers, L. Mercury, P. Fenter, & M. Hochella (Eds.), *Physicochemistry of Water in Geological and Biological Systems* (pp. 129–158). Tokyo: Univ. Acad. Press, Inc.
- Stauble, A. J., & Milius, G. (1970). Geology of Groningen gas field, Netherlands. In M. T. Halbouty (Ed.), *Geology of giant petroleum fields* (Vol. 14, pp. 359–369). Tulsa: American Association of Petroleum Geologists Memoir.
- Tse, S. T., & Rice, J. R. (1986). Crustal earthquake instability in relation to the depth variation of frictional slip properties. *Journal of Geophysical Research*, *91*(B9), 9452. <https://doi.org/10.1029/JB091iB09p09452>
- Tullis, T. E., & Weeks, J. D. (1986). Constitutive behavior and stability of frictional sliding of granite. *Pure and Applied Geophysics* *PAGEOPH*, *124*(3), 383–414. <https://doi.org/10.1007/BF00877209>
- Tullis, T. E., & Weeks, J. D. (1987). Micromechanics of frictional resistance of calcite. *Eos, Transactions American Geophysical Union*, *68*, 405.
- Valoroso, L., Chiaraluze, L., Piccinini, D., Di Stefano, R., Schaff, D., & Waldhauser, F. (2013). Radiography of a normal fault system by 64,000 high-precision earthquake locations: The 2009 L'Aquila (central Italy) case study. *Journal of Geophysical Research: Solid Earth*, *118*, 1156–1176. <https://doi.org/10.1002/jgrb.50130>
- van Thienen-Visser, K., & Breunese, J. N. (2015). Induced seismicity of the Groningen gas field: History and recent developments. *The Leading Edge*, *34*(6), 664–671. <https://doi.org/10.1190/le34060664.1>
- Verberne, B. A. (2015). Strength, stability, and microstructure of simulated calcite faults sheared under laboratory conditions spanning the brittle-plastic transition, Utrecht University.
- Verberne, B. A., Spiers, C. J., Niemeijer, A. R., de Bresser, J. H. P., de Winter, D. A. M., & Plümpner, O. (2013). Frictional properties and microstructure of calcite-rich fault gouges sheared at sub-seismic sliding velocities. *Pure and Applied Geophysics*, *171*, 2617–2640. <https://doi.org/10.1007/s00024-013-0760-0>
- Wassing, B., Buijze, L., & Orlic, B. (2017). The impact of visco-elastic caprock on fault reactivation and fault rupture in producing gas fields, *Schatzalp 2nd Induc. Seism. Work*.
- Zhang, X., Spiers, C. J., & Peach, C. J. (2010). Compaction creep of wet granular calcite by pressure solution at 28 °C to 150 °C. *Journal of Geophysical Research*, *115*, B09217. <https://doi.org/10.1029/2008JB005853>